

A Control Allocation Algorithm for Hypersonic Glide Vehicles with Input Limitations

Johannes Autenrieb*

German Aerospace Center (DLR), Institute of Flight Systems, 38108, Braunschweig, Germany

Patrick Gruhn†

German Aerospace Center (DLR), Institute of Aerodynamics and Flow Technology, 51147, Cologne, Germany

Hypersonic glide vehicles (HGVs) operate in challenging flight regimes characterized by strong nonlinearities in actuation and stringent physical constraints. These include state-dependent actuator limitations, asymmetric control bounds, and thermal loads that vary with maneuvering conditions. This paper introduces an iterative control allocation method to address these challenges in real time. The proposed algorithm searches for control inputs that achieve the desired moment commands while respecting constraints on input magnitude and rate. For slender HGV configurations, thermal loads and drag generation are strongly correlated—lower drag typically results in reduced surface heating. By embedding drag-sensitive soft constraints, the method improves energy efficiency and implicitly reduces surface temperatures, lowering the vehicle’s infrared signature. These features are particularly advantageous for long-range military operations that require low observability. The approach is demonstrated using the DLR’s Generic Hypersonic Glide Vehicle 2 (GHGV-2) simulation model. The results confirm the method’s effectiveness in maintaining control authority under realistic, constrained flight conditions.

Nomenclature

Symbols

B	= Control effectiveness matrix, $\mathbb{R}^{3 \times 4}$
$B_{\nu_x}, B_{\nu_y}, B_{\nu_z}$	= Conditionalized rows of B associated with roll, pitch, and yaw
C_D	= Aerodynamic drag coefficient
D	= Attainable moment set, \mathbb{R}^3
J	= Allocation cost, $J = \ \mathbf{u}\ _2^2$
$\mathbf{L} = [L, M, N]^T$	= Body-axis moment vector (roll, pitch, yaw) in Nm
N_{iter}	= Number of iterations in IDCA loop

*Research Scientist, Department of Flight Dynamics and Simulation, email:johannes.autenrieb@dlr.de

†Head of Missile Technologies Group, Department of Supersonic and Hypersonic Technologies, email:patrick.gruhn@dlr.de

P	= Cost matrix in quadratic program
q	= Dynamic pressure in N/m ²
r	= Relative degree of the output
T	= Time step in s
u	= Control input vector, \mathbb{R}^4
u_i	= Control input for effector i in deg
\dot{u}_i	= Rate of control input i in deg/s
$u_{\max,i}$	= Upper magnitude bound for u_i in deg
$u_{\min,i}$	= Lower magnitude bound for u_i in deg
$\dot{u}_{\max,i}$	= Upper rate bound for u_i in deg/s
$\dot{u}_{\min,i}$	= Lower rate bound for u_i in deg/s
u_s	= Desired steady-state control input vector
u_r	= Baseline control input from trajectory planning
$\Delta\mathbf{u}$	= Control input correction vector
ν	= Virtual control input vector, \mathbb{R}^3
ν_x, ν_y, ν_z	= Components of ν , corresponding to roll (L), pitch (M), and yaw (N)
$\Delta\nu$	= Corrective virtual control command
x	= State vector, \mathbb{R}^n
y	= Output vector, \mathbb{R}^p
h(x)	= Output mapping, $\mathbb{R}^n \rightarrow \mathbb{R}^p$
$L_i \mathbf{h}$	= Lie derivative of function h along vector field i (e.g. f , g)
α	= Angle of attack in rad
β	= Sideslip angle in rad
γ	= Flight path angle in rad
ρ	= Atmospheric air density in kg/m ³
$\Lambda(t)$	= Time-dependent modulation of input constraints
σ	= Operating point vector (e.g. altitude, Mach number)

Subscripts

c	= Command or control
r	= Reference or baseline input
s	= Steady-state solution

i = Index for control surface or effector

\max = Maximum bound

\min = Minimum bound

iter = Iteration index

I. Introduction

In recent years, hypersonic glide vehicles (HGVs) have received increasing attention in academic and industrial research and development [1]. These vehicles, designed to navigate through lower atmospheric layers at hypersonic speeds, present unique challenges that require precise control for optimal performance and guaranteed stability. Some HGV designs incorporate redundant control effectors, necessitating a control allocation system capable of distributing desired forces and moments among a redundant set of control effectors to achieve the desired vehicle response [2].

Traditional control allocation methods for overactuated aerial vehicles have evolved significantly. For most aerospace applications, the pseudoinverse-based control allocation (PICA) method [3], utilizing the Moore-Penrose inverse, is commonly used due to its simplicity. However, PICA does not adequately account for control input limitations. An alternative and more precise approach is to formulate the constrained control allocation problem as a quadratic programming (QPCA) problem and solve it using a QP solver [4, 5]. This method can accurately handle asymmetric input constraints and coupling effects between control effectors. However, the computational intensity of QP solvers poses significant challenges for real-time implementation on systems with limited computational resources, such as embedded systems in hypersonic reentry vehicles [6]. The high computational demand makes it difficult to guarantee real-time performance, which is essential for the fast dynamics of HGVs. To address the need for a computationally less complex solution, Bordignon introduced the redistributed pseudoinverse control allocation (RPICA) method [7]. RPICA iteratively approximates feasible solutions by redistributing residuals over the attainable moment set (AMS), offering a balance between computational efficiency and practicality. A scaled variant, RSPICA, was later proposed to maintain the directionality of the input vector in multiple-input, multiple-output (MIMO) systems under saturation conditions. Despite advancements in computational simplicity, both RPICA and RSPICA face challenges when dealing with systems characterized by asymmetric control input limits and strong inter-directional coupling between control effectors. This issue is particularly evident in certain classes of HGVs where only positive control deflections are permissible. The inability of these methods to effectively handle asymmetric constraints and coupling effects limits their applicability in such scenarios.

Over the past few years, the German Aerospace Center (DLR) has undertaken a substantial research initiative focused on the development of the Generic Hypersonic Glide Vehicle 2 (GHGV-2). This research aims to comprehensively explore the capabilities and performance characteristics of strategic hypersonic glide vehicles, shedding light on their

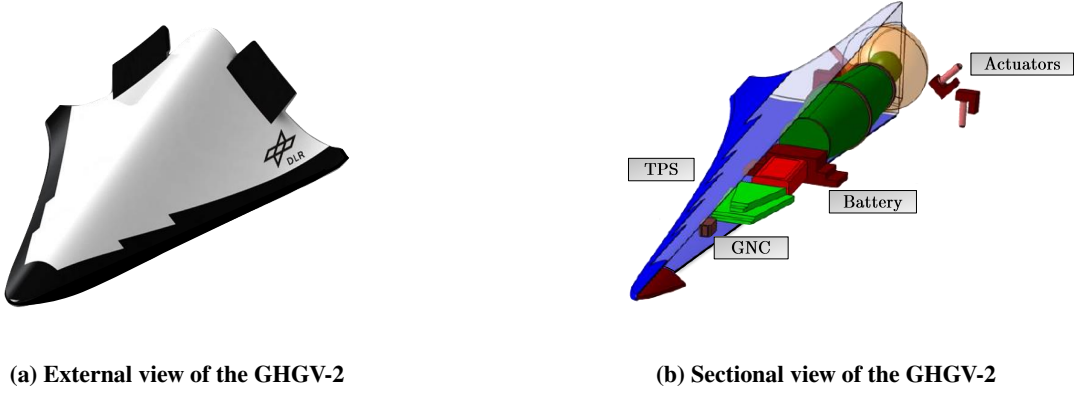


Figure 1 The DLR Generic Hypersonic Glide Vehicle 2 concept.

implications for understanding hypersonic threats [8, 9]. The GHGV-2 adopts a waverider design to optimize lift-to-drag ratios at high Mach numbers [10]. The GHGV-2 is depicted in Figure 1, with an external view shown in Figure 1a and a sectional view highlighting relevant subsystems in Figure 1b. Key subsystems include the thermal protection system (TPS), guidance, navigation, and control (GNC) system, battery, and actuators. During endoatmospheric flight, the GHGV-2 utilizes four integrated flaps as control effectors to regulate its attitude. Small propulsors are integrated in exoatmospheric conditions to generate the necessary moments for attitude adjustments.

The GHGV-2 is launched via a multi-stage rocket booster as part of the investigated mission profile. After ignition and acceleration, the vehicle separates from the launch system at an altitude of approximately 100 km, initiating a parabolic re-entry trajectory. Once sufficient dynamic pressure is achieved during descent, the vehicle transitions to aerodynamic control using four surfaces, two located on the upper and two on the lower side. Following re-entry, the GHGV-2 tracks a predefined flight path angle to sustain its maximum lift-to-drag ratio en route to the target location. Due to sustained hypersonic speeds, the vehicle is exposed to significant thermal loads during this atmospheric glide phase. Consequently, any viable control allocation algorithm must generate the necessary control moments for maneuvering and account for thermal effects, ideally minimizing heat loads to reduce the burden on the TPS and lower the infrared signature, a key consideration for military applications. Another critical challenge arises from state-dependent control input limitations stemming from the wide range of operating conditions. Increased dynamic pressure at lower altitudes and higher speeds restricts actuator authority compared to flight conditions involving lower speeds or air densities. This variability demands a control allocation approach explicitly incorporating state-dependent constraints to ensure robust actuator performance throughout the mission.

Given these complexities, developing a control allocation algorithm that is both computationally efficient for real-time implementation on embedded systems and capable of handling asymmetric control input limitations, actuator coupling, thermal load considerations, and state-dependent constraints is a significant challenge. This work presents an iterative control allocation approach explicitly tailored for hypersonic glide vehicles like the GHGV-2. We begin

with introducing the general control allocation problem of overactuated systems and then discuss the specific control allocation problem for HGVs, highlighting the unique challenges posed by asymmetric control input limitations, significant coupling between control effectors, thermal load considerations, and state-dependent actuator constraints due to varying flight conditions. Based on the described problem formulation, we present our proposed method that addresses these challenges by directly incorporating state-dependent control input limits and thermal load considerations into the control allocation algorithm. It iteratively adjusts the control inputs to ensure the required control moments are achieved while respecting all constraints and minimizing thermal stress on the control surfaces. The algorithm is designed to be computationally efficient, making it suitable for real-time implementation on the vehicle's embedded systems. We evaluate the effectiveness of the proposed approach through numerical simulations, demonstrating its advantages in handling the complex requirements of hypersonic glide vehicle control allocation. The results show that our method provides a reliable solution that balances computational efficiency with the ability to manage asymmetric constraints, actuator coupling, and thermal considerations.

II. The General Control Allocation Problem

We define the following nonlinear control-affine system

$$\dot{\mathbf{x}}(t) = \mathbf{f}(\mathbf{x}(t)) + \mathbf{g}(\mathbf{x}(t))\mathbf{u}(t), \quad (1)$$

$$\mathbf{y}(t) = \mathbf{h}(\mathbf{x}(t)), \quad (2)$$

where $\mathbf{x}(t) \in \mathbb{R}^n$, $\mathbf{u}(t) \in \mathbb{R}^m$ and $\mathbf{y}(t) \in \mathbb{R}^p$. The function $\mathbf{f} : \mathbb{R}^n \rightarrow \mathbb{R}^n$ represents a Lipschitz continuous system function, $\mathbf{h} : \mathbb{R}^n \rightarrow \mathbb{R}^p$ a Lipschitz continuous output function, and $\mathbf{g}(\mathbf{x}(t)) \in \mathbb{R}^{n \times m}$ is referred to as the control effectiveness matrix. In the field of flight control, inversion-based control methodologies, such as NDI, are commonly used to impose desired closed-loop behavior on the MIMO dynamics [11]. To do so, the time derivatives of the introduced nonlinear dynamics from Eq. (1) and Eq. (2) are derived and reformulated using the Lie derivative notation [12]:

$$\begin{aligned} \dot{\mathbf{y}}(t) &= \frac{\partial \mathbf{h}}{\partial \mathbf{x}} \dot{\mathbf{x}}(t) = \frac{\partial \mathbf{h}}{\partial \mathbf{x}} [\mathbf{f}(\mathbf{x}(t)) + \mathbf{g}(\mathbf{x}(t))\mathbf{u}(t)] \\ &= \frac{\partial \mathbf{h}}{\partial \mathbf{x}} \mathbf{f}(\mathbf{x}(t)) + \frac{\partial \mathbf{h}}{\partial \mathbf{x}} \mathbf{g}(\mathbf{x}(t)) \mathbf{u}(t) \\ &= L_{\mathbf{f}} \mathbf{h}(\mathbf{x}(t)) + L_{\mathbf{g}} \mathbf{h}(\mathbf{x}(t)) \mathbf{u}(t) \\ &= \mathbf{F}(\mathbf{x}(t)) + \mathbf{G}(\mathbf{x}(t)) \mathbf{u}(t). \end{aligned} \quad (3)$$

A relationship between the input and the output can be established if $\mathbf{G}(\mathbf{x}(t)) \neq 0$. For cases in which $\mathbf{G}(\mathbf{x}(t)) = 0$, the relationship must be further derived until the system input affects the system output. The number of time derivations

needed is called the relative degree and is represented by r [13]. For the sake of brevity, we consider here an example of a first-order system. For such a system with a relative degree of one, the NDI-based control law can be stated as:

$$\mathbf{u}(t) = \mathbf{G}(\mathbf{x}(t))^{-1} [\mathbf{v}(t) - \mathbf{F}(\mathbf{x}(t))], \quad (4)$$

with $\mathbf{v}(t) \in \mathbb{R}^o$ being a virtual control input vector created by a linear controller to impose the desired closed-loop characteristics on the controlled variables such that $\mathbf{v}(t) = -\mathbf{K}\mathbf{y}(t)$, with \mathbf{K} being a Hurwitz gain matrix. It is evident that the inversion of the control effectiveness matrix $\mathbf{G}(\mathbf{x}(t))$, from now on for simplicity referred to as \mathbf{B} , maps a desired $\mathbf{v}(t)$ into the control space \mathbb{R}^m . In cases in which $m = n$ and $\text{rank}(\mathbf{B}) = n$, this leads to a unique solution. In the case of over-actuation, where $m > n$, the inversion of the matrix is not easily available, since the mapping into the control space is not unique and, mathematically speaking, under-determined. In the flight control literature this problem is often referred to as the control allocation problem [14]. In general, the control allocation problem can be interpreted as a constrained optimization problem since magnitude and rate limitations on each actual available control effector $u_i(t)$ need to be considered. The rate limits are often defined as symmetric lower and upper bounds for each actuator, leading to the following rate saturation function for each actuator i :

$$R(\dot{u}_i(t)) = \begin{cases} \dot{u}_{\max,i}, & \text{if } \dot{u}_i(t) > \dot{u}_{\max,i}, \\ \dot{u}_{\min,i}, & \text{if } \dot{u}_i(t) < \dot{u}_{\min,i}, \\ \dot{u}_i(t), & \text{else.} \end{cases} \quad (5)$$

Since a small and constant time step T for the control computation can be assumed, the rate limits can be interpreted as additional rate-dependent magnitude limits $\bar{u}_i(t)$ relative to the current deflection state $u_i(t)$, modeled as a zero-order hold limit:

$$\bar{u}_i(t) = u_i(t - T) + R(\dot{u}_i(t)) T. \quad (6)$$

Based on that, the magnitude limitations can be defined as individual lower and upper bounds for each effector i . The magnitude-constrained control inputs are represented using the following magnitude saturation function:

$$S(u_i(t), \dot{u}_i(t)) = \begin{cases} \min(u_{\max,i}, \bar{u}_i(t)), & \text{if } u_i(t) \geq \min(u_{\max,i}, \bar{u}_i(t)), \\ \max(u_{\min,i}, \bar{u}_i(t)), & \text{if } u_i(t) < \max(u_{\min,i}, \bar{u}_i(t)), \\ u_i(t), & \text{else.} \end{cases} \quad (7)$$

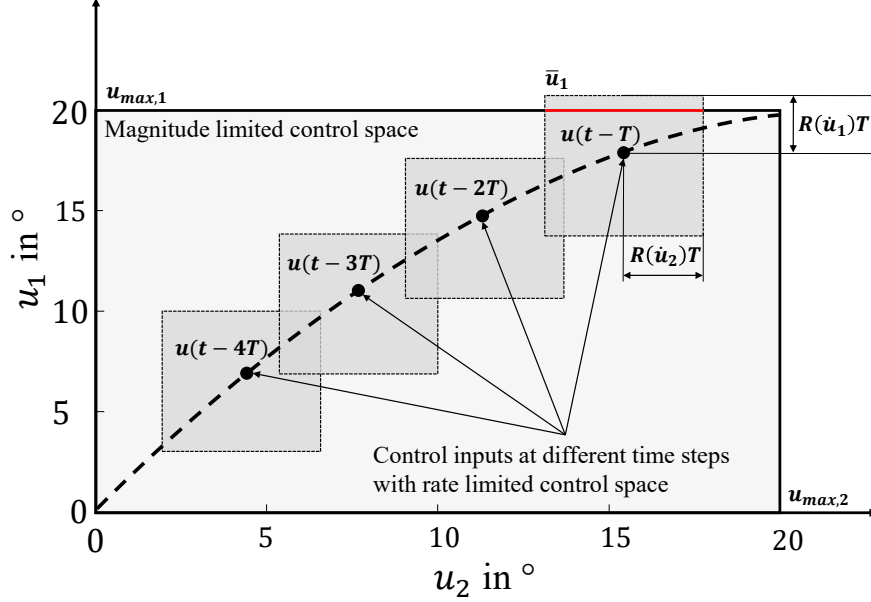


Figure 2 Illustration of the discussed control allocation problem with considered magnitude and rate limits for a system with two control inputs u_1 and u_2 .

This leads to the following formulation of the feasible set of control inputs \mathbf{U} :

$$\mathbf{U} := \{\mathbf{u}(t) \in \mathbb{R}^m \mid \forall i \in [1, m] : \max(u_{\min,i}, \bar{u}_i(t)) \leq u_i(t) \leq \min(u_{\max,i}, \bar{u}_i(t))\}. \quad (8)$$

The described admissible control input space for a static toy example with two magnitude- and rate-constrained control inputs u_1 and u_2 is given in Fig. 2.

Based on the feasible set of control inputs, a feasible physical control volume \mathbf{D} can be constructed as

$$\mathbf{D} := \{\mathbf{v}(t) \in \mathbb{R}^o \mid \mathbf{v}(t) = \mathbf{B}\mathbf{u}(t), \mathbf{u}(t) \in \mathbf{U}\}. \quad (9)$$

In the context of flight control, the resulting convex set \mathbf{D} is often referred to as the attainable moment set (AMS) [15]. An example of an AMS, in which dynamic effects coming from the rate limits are neglected, for a hypersonic glide vehicle with four control effectors ($m = 4$) is shown in Fig. 3.

The resulting general control allocation problem, considering magnitude and rate limits on the control input, can be

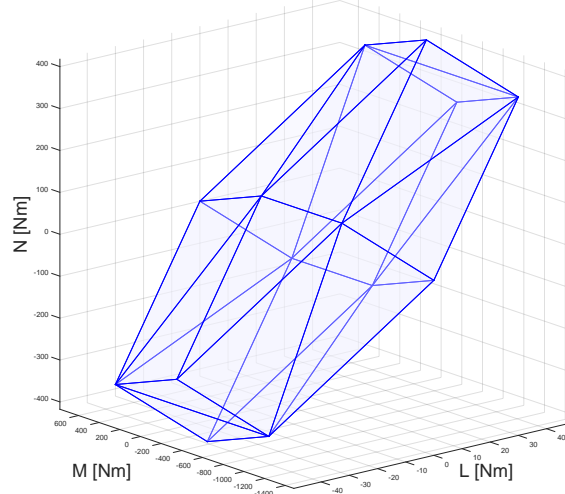


Figure 3 An exemplary plot of an attainable moment set of the GHGV-2 for an operating point at $M = 8$ and $H = 30$ km.

formulated as the following constrained optimization problem:

$$\begin{aligned}
 \arg \min_{\mathbf{u}(t) \in \mathbb{R}^m} \quad & \|\mathbf{u}(t)\|_p & (10) \\
 \text{subject to} \quad & \mathbf{v}(t) = \mathbf{B}\mathbf{u}(t), \\
 & \max(\mathbf{u}_{\min}, \bar{\mathbf{u}}(t)) \leq \mathbf{u}(t) \leq \min(\mathbf{u}_{\max}, \bar{\mathbf{u}}(t)),
 \end{aligned}$$

with p being a real number used to define the considered norm. In this work and without further discussion, the ℓ_2 -norm was chosen. Approaches based on the ℓ_1 -norm or the ℓ_∞ -norm could also lead to desirable results; interested readers are referred to [14, 16–19] for deeper discussions on the topic of the influence of different norms on the control allocation performance. Based on the decision to minimize the ℓ_2 -norm of the least-square problem, the optimization problem can be formulated as a quadratic programming control allocation (QPCA) problem [4, 5].

A. Control Allocation Algorithms

This section presents a brief overview of three commonly used algorithms in control allocation, highlighting their benefits and limitations in distributing virtual control input commands for the considered class of overactuated hypersonic systems.

1. Pseudoinverse-Based Control Allocation

The majority of the control allocation problems are solved by pseudoinverse-based control allocation (PICA) using the Moore-Penrose pseudoinverse, which provides the min-norm solution and which implicitly solves the following

unconstrained least-square problem for the allocation of the incremental virtual control input vector ν :

$$\begin{aligned} \min_{\mathbf{u} \in \mathbb{R}^m} \quad & \|\mathbf{u}\|_2 \\ \text{subject to} \quad & \nu = \mathbf{B}\mathbf{u}, \end{aligned} \quad (11)$$

with $\|\cdot\|_2$ being the ℓ_2 -norm. The defined optimization problem has the following closed-form solution:

$$\mathbf{u} = \mathbf{B}^+ \nu = \mathbf{B}^T [\mathbf{B}\mathbf{B}^T]^{-1} \nu. \quad (12)$$

The major drawback of the generalized inverse approach is that the constraints on the control input \mathbf{u} are neglected, leading to the computation of possibly infeasible control inputs.

2. *Redistributed Pseudoinverse-Based Control Allocation*

An alternative approach to solve the constrained control allocation problem was proposed by the authors in [20] and is called redistributed pseudoinverse-based control allocation (RPICA). The core idea of the methodology is to cope with the problem of limited control input authority by iterating over the AMS until a feasible control input command is found. The algorithm starts by generating a first solution for a control vector candidate using the pseudoinverse

$$\mathbf{u}^{(1)} = \mathbf{B}^+ \nu^{(0)}, \quad (13)$$

with $\nu^{(0)}$ being the initially desired commanded virtual control input vector from the controller. In the case where no element of $\mathbf{u}^{(1)}$ is saturated, and Eq. (7) delivers the desired virtual control input vector, $\mathbf{u}^{(1)}$ is the final solution. In cases where at least one element of $\mathbf{u}^{(1)}$ conflicts with the available control limitations and the desired virtual control input vector is not generated, the process continues. The achievable control input is defined as

$$\nu^{(1)} = \mathbf{B} S(\mathbf{u}^{(1)}), \quad (14)$$

with $S(\mathbf{u}^{(1)})$ being a simplified version of the magnitude saturation function defined in Eq. (7), since in most of the formulations in the existing literature the rate limits are neglected. The control effectiveness matrix \mathbf{B} is then sparsified such that the matrix columns which correspond to the saturated actuators are zeroed. Also, the limits are adjusted to make sure that the final solution does not exceed the actual bounds:

$$\mathbf{u}_{\max}^{(j)} = \mathbf{u}_{\max}^{(j-1)} - \mathbf{u}^{(j)}, \quad (15)$$

$$\mathbf{u}_{\min}^{(j)} = \mathbf{u}_{\min}^{(j-1)} - \mathbf{u}^{(j)}. \quad (16)$$

Now, the remaining pseudo-control vector is computed as

$$\mathbf{v}^{(j)} = \mathbf{v}^{(j-1)} - \mathbf{B}_s S(\mathbf{u}^{(j)}), \quad (17)$$

with \mathbf{B}_s being the sparsified control effectiveness matrix. In the next iteration step, the remaining pseudo-control vector is allocated using \mathbf{B}_s and the adjusted limits as defined in Eq. (15) and Eq. (16). That procedure is continued until either the desired pseudo-control vector has been achieved or the maximum number of iterations has been reached. In both cases, the final control vector is the sum of the increments of all iteration steps.

For MIMO systems, it is preferable to keep the directionality of the unconstrained input vector $\mathbf{u}^{(j)}$. To make that possible, the authors in [21] proposed the redistributed scaling pseudoinverse control allocation (RSPICA) algorithm. The saturated control input vector is scaled within the method to ensure perfect direction alignment with the desired pseudo-control vector. The used scalar a is chosen such that the element that exceeds its respective limit the most is saturated, while the others are not:

$$\mathbf{u}_a^{(j)} = \underbrace{\min \left(1, \frac{l(u_1^{(j-1)})}{u_1^{(j)}}, \frac{l(u_2^{(j-1)})}{u_2^{(j)}}, \dots, \frac{l(u_m^{(j-1)})}{u_m^{(j)}} \right)}_a \cdot \mathbf{u}^{(j)}, \quad (18)$$

with

$$l(u_i^{(j-1)}) = \begin{cases} u_{\max,i}^{(j-1)}, & \text{if } u_i^{(j)} > 0, \\ u_{\min,i}^{(j-1)}, & \text{if } u_i^{(j)} < 0. \end{cases}$$

Both RPICA and its scaled variant, RSPICA, are advantageous for implementation in embedded systems with limited computational resources due to their simplicity. RSPICA, in particular, was designed to maintain input vector directionality in MIMO systems under saturation conditions by scaling the requested vector with a factor a , thereby ensuring that control input constraints are respected. However, despite these advancements, both methods have notable limitations. Their reliance on the ℓ_2 -based least-squares approach, inherent in the Moore-Penrose pseudoinverse, can result in an inefficient use of the AMS, when the asymmetrical input constraints and strong inter-directional control authority of the control effectors are present. Additionally, for systems with asymmetric input limits where the lower input bound is zero, RSPICA may produce zero-scaled solutions, resulting in trivial control commands. These challenges are particularly problematic for the here considered class of HGVs.

3. Quadratic Programming-Based Control Allocation

The constrained control allocation problem can also be solved using a quadratic programming-based control allocation (QPCA) approach. Examples of that can be found in the work presented in [4] and [22]. To discuss this, we introduce the general formulation of a quadratic programming problem

$$\begin{aligned} \min_{\mathbf{x}} \quad & \frac{1}{2} \mathbf{x}^T \mathbf{P} \mathbf{x} + \mathbf{q}^T \mathbf{x} \\ \text{subject to} \quad & \mathbf{A} \mathbf{x} \leq \mathbf{b}, \end{aligned} \quad (19)$$

with $\mathbf{A} \mathbf{x} \leq \mathbf{b}$ being a linear matrix inequality to constrain the solution of \mathbf{x} . In the context of control allocation, we often aim to solve the following constrained weighted least-squares problem:

$$\begin{aligned} \min_{\mathbf{u}} \quad & \frac{1}{2} \|\mathbf{B} \mathbf{u} - \mathbf{v}\|_{\mathbf{W}}^2 \\ \text{subject to} \quad & \mathbf{A}_u \mathbf{u} \leq \mathbf{b}_u, \end{aligned} \quad (20)$$

with $\mathbf{A}_u \mathbf{u} \leq \mathbf{b}_u$ reflecting control limits, and $\|\mathbf{y}\|_{\mathbf{W}} = \sqrt{\mathbf{y}^T \mathbf{W} \mathbf{y}}$ being a weighted form of the Euclidean norm for a vector \mathbf{y} . We can introduce a conversion of the least-squares cost function to a quadratic programming objective by

$$\begin{aligned} \|\mathbf{B} \mathbf{u} - \mathbf{v}\|_{\mathbf{W}}^2 &= (\mathbf{B} \mathbf{u} - \mathbf{v})^T \mathbf{W} (\mathbf{B} \mathbf{u} - \mathbf{v}) \\ &= \mathbf{u}^T \mathbf{B}^T \mathbf{W} \mathbf{B} \mathbf{u} - 2 \mathbf{u}^T \mathbf{B}^T \mathbf{W} \mathbf{v} + \mathbf{v}^T \mathbf{W} \mathbf{v}. \end{aligned} \quad (21)$$

Since the term $\mathbf{v}^T \mathbf{W} \mathbf{v}$ is constant and independent of \mathbf{u} , it can be discarded. This yields

$$\|\mathbf{B} \mathbf{u} - \mathbf{v}\|_{\mathbf{W}}^2 \propto \mathbf{u}^T \mathbf{B}^T \mathbf{W} \mathbf{B} \mathbf{u} - 2(\mathbf{B}^T \mathbf{W} \mathbf{v})^T \mathbf{u}. \quad (22)$$

Multiplying by $\frac{1}{2}$ gives the final quadratic form

$$\frac{1}{2} \mathbf{u}^T \mathbf{B}^T \mathbf{W} \mathbf{B} \mathbf{u} - (\mathbf{B}^T \mathbf{W} \mathbf{v})^T \mathbf{u}, \quad (23)$$

which corresponds to a quadratic programming problem with

$$\mathbf{P} = \mathbf{B}^T \mathbf{W} \mathbf{B}, \quad \mathbf{q} = -\mathbf{B}^T \mathbf{W} \mathbf{v}. \quad (24)$$

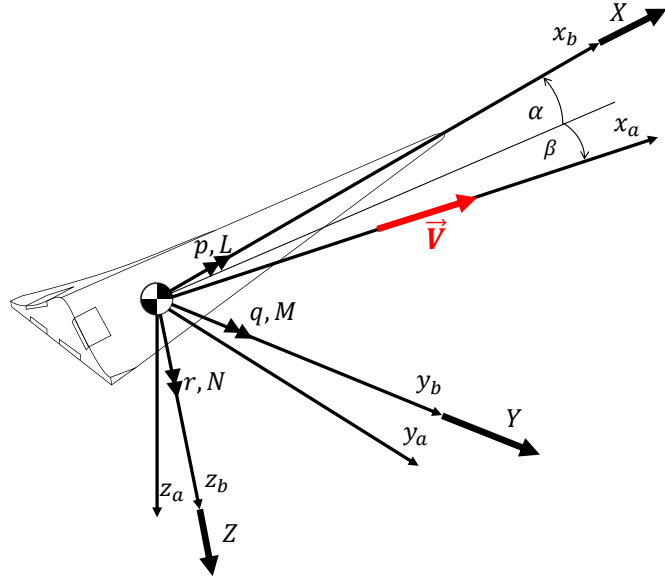


Figure 4 Sketch of external forces and moments acting on the GHGV-2 concept.

The constrained QPCA problem can therefore be formulated as

$$\begin{aligned} \arg \min_{\mathbf{u} \in \mathbb{R}^m} \quad & \frac{1}{2} \mathbf{u}^T \mathbf{B}^T \mathbf{W} \mathbf{B} \mathbf{u} - (\mathbf{B}^T \mathbf{W} \mathbf{v})^T \mathbf{u} \\ \text{subject to} \quad & \mathbf{A}_u \mathbf{u} \leq \mathbf{b}_u, \end{aligned} \quad (25)$$

with $\mathbf{A}_u = [\mathbf{I}_{m \times m}, -\mathbf{I}_{m \times m}]^T$ and $\mathbf{b}_u = [\min(u_{\max,i}, \bar{u}_i), -\max(u_{\min,i}, \bar{u}_i)]^T$. The formulated QPCA problem can be solved using a variety of methods, such as interior-point, active-set, or simplex [5]. The advantage of the method is that it is able to provide solutions to complex control allocation problems. However, a significant drawback of the approach is the high computational complexity and with that the lack of real-time guarantees for certain embedded systems integrated in aerial vehicles, for example the system integrated into the GHGV-2.

III. Problem Formulation

The considered GHGV-2 is modeled as a rigid body, and the nonlinear flight dynamics of the HGV are based on classical Newtonian mechanics.

Figure 4 displays the components X , Y , Z of the total external force vector and the components L , M , N of the total external moment vector expressed in the body-fixed frame of the vehicle. As detailed in Section II, the application of suitable control allocation algorithms is essential for the over-actuated GHGV-2, both in exoatmospheric and endoatmospheric flight phases.

Due to the brevity of this paper, we limit our discussion to the control allocation problem during the endoatmospheric

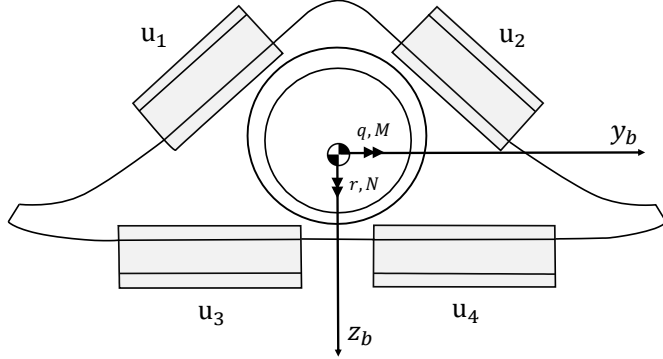


Figure 5 Rear view of the GHGV-2 showing available control effectors during endoatmospheric operations [23].

flight phase. In this context, only the aerodynamic and gravitational forces and moment effects are relevant for the considered problem and the later presented results.

Figure 5 illustrates the available aerodynamic control surfaces and their corresponding deflections: upper left fin u_1 , upper right fin u_2 , lower left fin u_3 , and lower right fin u_4 . This leads to the following control input vector

$$\mathbf{u}(t) = \begin{bmatrix} u_1(t) & u_2(t) & u_3(t) & u_4(t) \end{bmatrix}^T. \quad (26)$$

The aerodynamic coefficient derivatives with respect to the control surface deflections can be fairly well approximated by linear terms. To account for the dependencies on the current flight state $\mathbf{x}(t)$ and the operating point $\sigma(t)$, the control effectiveness matrix $\mathbf{B}(\mathbf{x}(t), \sigma(t))$ is continuously re-computed using an onboard plant model and sensor measurements. However, it is assumed to be constant within each time step. The control effectiveness matrix $\mathbf{B}(\mathbf{x}(t), \sigma(t))$ with respect to a virtual control command input vector $\mathbf{v}(t) = [v_x(t), v_y(t), v_z(t)]^T$ is thus defined as:

$$\mathbf{B}(\mathbf{x}(t), \sigma(t)) = \begin{bmatrix} \frac{\partial v_x}{\partial u_1} & \frac{\partial v_x}{\partial u_2} & \frac{\partial v_x}{\partial u_3} & \frac{\partial v_x}{\partial u_4} \\ \frac{\partial v_y}{\partial u_1} & \frac{\partial v_y}{\partial u_2} & \frac{\partial v_y}{\partial u_3} & \frac{\partial v_y}{\partial u_4} \\ \frac{\partial v_z}{\partial u_1} & \frac{\partial v_z}{\partial u_2} & \frac{\partial v_z}{\partial u_3} & \frac{\partial v_z}{\partial u_4} \end{bmatrix}, \quad (27)$$

with $\mathbf{B}(\mathbf{x}(t), \sigma(t)) \in \mathbb{R}^{3 \times 4}$. As it is a non-square matrix, it cannot be inverted directly.

A major challenge in hypersonic flights, often neglected in the literature, is the dependence of actuator magnitude and rate limits not only on the instantaneous flight state $\mathbf{x}(t)$ but also on the operating point $\sigma(t)$. During high-speed atmospheric operations, high dynamic pressure induces counterforces on actuators, limiting the achievable deflections and rates. Nonlinear aerodynamic effects further complicate matters, with asymmetric influences on upper and

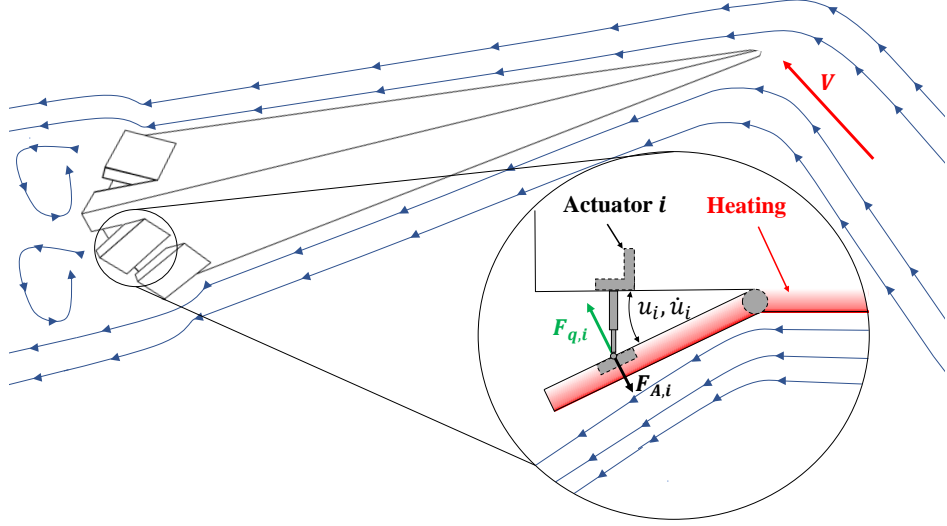


Figure 6 Illustration of an overactuated hypersonic glide vehicle during high-speed atmospheric operations with high dynamic pressure and thermal loads.

lower surfaces requiring distinct actuator constraints. Additionally, operating-point-dependent thermal loads must be considered to minimize heating, reduce the burden on the TPS, and lower the infrared signature of the vehicle during operations.

These effects are illustrated in Fig. 6. In this figure, the red arrow \mathbf{V} represents the resulting velocity vector of the vehicle as it moves at high speed through the atmosphere. The blue arrows depict the airflow vector fields around the vehicle, shaping the aerodynamic forces and heating effects on the control surfaces. The control surface i , modeled as a flapping plate, is characterized by a deflection angle u_i and a deflection rate \dot{u}_i . The red gradient along the control surface indicates aerodynamic heating, generated by the vehicle's hypersonic speed, causing significant heat flux τ_i on the surface. These heating effects must be considered during operation to avoid material degradation and structural failure of the control surfaces and to minimize the infrared signature in defense scenarios. The green arrow $\mathbf{F}_{q,i}$ represents the normal of the aerodynamic force acting on the surface, which is highly dependent on the deflection angle and the dynamic pressure $q = 0.5\rho V^2$ acting on the control surface area $S_{u,i}$, with ρ being the atmospheric density and V the resulting velocity. The actuator force $\mathbf{F}_{A,i}$ is responsible for controlling the position of the surface, working against $\mathbf{F}_{q,i}$, especially under high dynamic pressure conditions. Under these conditions, the actuator's ability to adjust the deflection angle and rate is sometimes restricted, leading to cases in which the deflection angle u_i is limited such that the resulting dynamic pressure force $F_{q,i}$ exceeds the maximum force that the actuator can provide.

To address these high Mach number effects, we define the control allocation problem as a constrained optimization problem with state- and operating-point-dependent magnitude and rate limitations. The rate saturation function for each

actuator i is defined as:

$$R(\dot{u}_i(t), \mathbf{x}(t), \boldsymbol{\sigma}(t)) = \begin{cases} \dot{u}_{\max,i}(\mathbf{x}(t), \boldsymbol{\sigma}(t)), & \text{if } \dot{u}_i(t) > \dot{u}_{\max,i}(\mathbf{x}(t), \boldsymbol{\sigma}(t)), \\ \dot{u}_{\min,i}(\mathbf{x}(t), \boldsymbol{\sigma}(t)), & \text{if } \dot{u}_i(t) < \dot{u}_{\min,i}(\mathbf{x}(t), \boldsymbol{\sigma}(t)), \\ \dot{u}_i(t), & \text{else.} \end{cases} \quad (28)$$

By modeling a rate-dependent magnitude limit \bar{u}_i relative to the current deflection state $\mathbf{u}(t)$, via Eq. (6), we can define a rate- and state-/operating-point-dependent magnitude saturation function:

$$S(u_i(t), \dot{u}_i(t), \mathbf{x}(t), \boldsymbol{\sigma}(t)) = \begin{cases} \min(u_{\max,i}(\mathbf{x}(t), \boldsymbol{\sigma}(t)), \bar{u}_i(t)), & \text{if } u_i(t) \geq \min(u_{\max,i}(\mathbf{x}(t), \boldsymbol{\sigma}(t)), \bar{u}_i(t)), \\ \max(u_{\min,i}(\mathbf{x}(t), \boldsymbol{\sigma}(t)), \bar{u}_i(t)), & \text{if } u_i(t) < \max(u_{\min,i}(\mathbf{x}(t), \boldsymbol{\sigma}(t)), \bar{u}_i(t)), \\ u_i(t), & \text{else.} \end{cases} \quad (29)$$

Leading to the following definition of the state- and operating-point-dependent feasible set of control inputs $\mathbf{U}(\mathbf{x}(t), \boldsymbol{\sigma}(t))$:

$$\mathbf{U}(\mathbf{x}(t), \boldsymbol{\sigma}(t)) := \{\mathbf{u}(t) \in \mathbb{R}^m \mid \forall i \in [1, m] : \max(u_{\min,i}(\mathbf{x}(t), \boldsymbol{\sigma}(t)), \bar{u}_i(t)) \leq u_i(t) \leq \min(u_{\max,i}(\mathbf{x}(t), \boldsymbol{\sigma}(t)), \bar{u}_i(t))\}. \quad (30)$$

A control allocation problem is formulated that not only considers the current control distribution at each time step, but also includes the previous time step as a soft constraint. This leads to the following constrained state- and operating-point-dependent optimization problem:

$$\begin{aligned} \min_{\mathbf{u}(t) \in \mathbb{R}^m} \quad & \|\mathbf{W}_m(\mathbf{u}(t) - \mathbf{u}_s(t))\|_2^2 + \|\mathbf{W}_r(\mathbf{u}(t) - \mathbf{u}(t-T))\|_2^2 \\ \text{subject to} \quad & \boldsymbol{\nu}(t) = \mathbf{B}(\mathbf{x}(t), \boldsymbol{\sigma}(t)) \mathbf{u}(t), \\ & \mathbf{u}(t) \in \mathbf{U}(\mathbf{x}(t), \boldsymbol{\sigma}(t)), \end{aligned} \quad (31)$$

with $\mathbf{u}_s(t)$ being a desired steady-state solution for a given virtual control input $\boldsymbol{\nu}(t)$. \mathbf{W}_m is a weighting matrix for the difference between the computed input and the desired steady-state solution, and \mathbf{W}_r is a weighting matrix for the delta between the computed control input $\mathbf{u}(t)$ and the control input of the previous time step $\mathbf{u}(t-T)$.

In summary, the problem addressed in this work is to find, at each time, a control input $\mathbf{u}(t)$ for the system defined in Eqs. (1) and (2), in accordance with Eq. (31), such that the virtual control input demand $\mathbf{B}(\mathbf{x}(t), \boldsymbol{\sigma}(t)) \mathbf{u}(t) = \boldsymbol{\nu}(t)$ is met if the command is within the state- and operating-point-dependent actuator limits. If the command is not feasible, the system should generate a command that minimizes the error between the requested and achievable command while

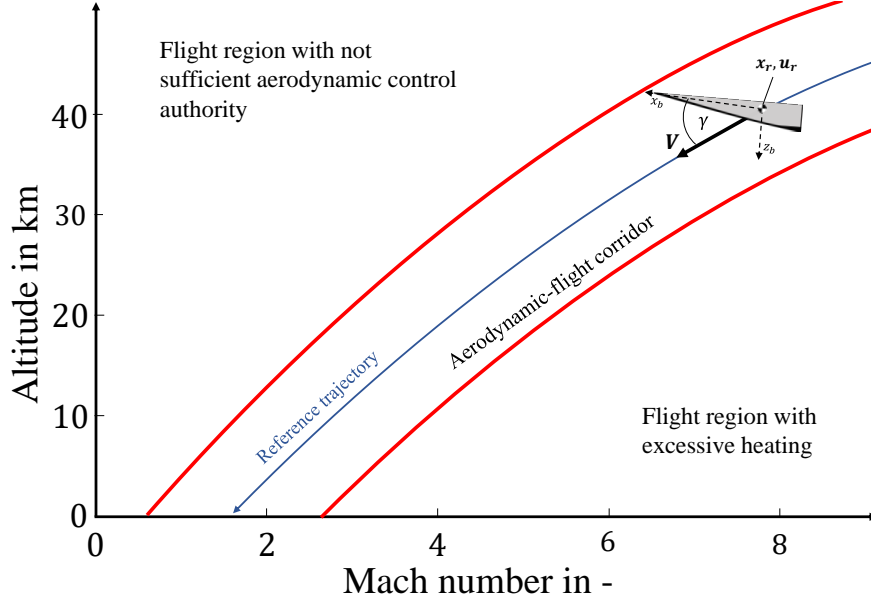


Figure 7 Illustration of an operational flight envelope for a hypersonic glide vehicle, showing the reference trajectory bounded by upper and lower limits.

respecting the input limitations from Eq. (30).

IV. The Integrated Overall Control Allocation Concept

As discussed in Sect. III, during atmospheric flight, HGVs face significant challenges in maintaining stability and control within a narrow altitude band due to either thermal loads or a lack of aerodynamic controllability [24]. These conditions complicate the design of effective control strategies and demand precise management of aerodynamic and thermal effects. Owing to this complexity, the atmospheric flight trajectory of the HGV is typically computed offline prior to the mission. During this offline optimization process, an optimal control problem is solved to ensure that, given specific initial and terminal conditions as well as physical constraints, a feasible trajectory is obtained [25].

The resulting optimized state reference trajectory is bounded by aerodynamic flight corridor constraints, as illustrated in Fig. 7. This figure provides an example of an operational flight corridor for a hypersonic glide vehicle and its associated reference trajectory. The corridor is defined by upper and lower Mach number limits as a function of altitude. When the vehicle ascends above the upper altitude bound, it enters a flight region with insufficient aerodynamic control authority due to reduced air density. Conversely, descending below the lower bound places the vehicle in a region with excessive heating, risking material degradation and structural failure. Based on the obtained state reference trajectory $x_r(t)$, an offline solution for the control input $u_r(t)$ is computed using a computationally demanding but accurate QP solver for the problem defined in Eq. (31), employing the methods discussed in Sect. II.A.3. This offline solution incorporates all known hard and soft actuator constraints, producing what is assumed to be the best solution for a

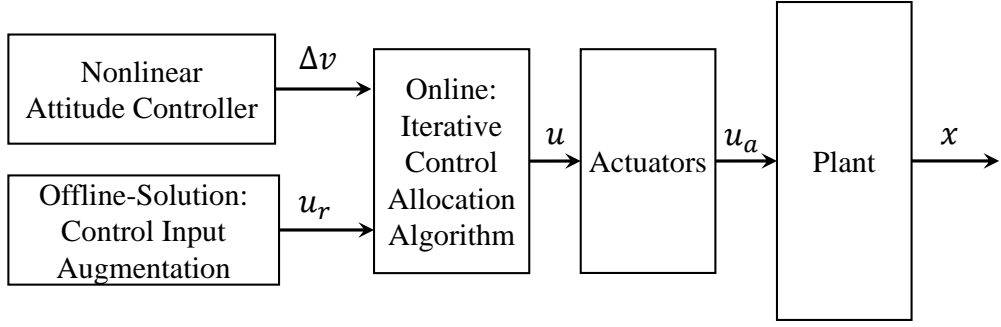


Figure 8 Concept of the integrated control allocation system for the GHGV-2.

disturbance-free environment. The computed control inputs from this offline optimization are stored in lookup tables and serve as baseline control inputs during flight.

The baseline control input $u_r(t)$ would be sufficient to maintain the vehicle on its reference trajectory in a scenario without external disturbances or model uncertainties. However, given the inherent uncertainties and potential disturbances in hypersonic flight, the control system also requires an attitude feedback controller to provide corrective actions [23]. This controller computes a corrective virtual control input $\Delta v(t)$ to compensate for deviations from the nominal trajectory due to unmodeled dynamics, uncertainties, and external disturbances. The proposed iterative online algorithm uses the virtual control input $\Delta v(t)$ to search in the attainable moment set (AMS) for a feasible control input $\Delta u(t)$. Assuming an affine structure for the control input, the final command can be expressed as a superposition of the offline baseline solution and the correction:

$$u(t) = u_r(t) + \Delta u(t). \quad (32)$$

The overall control allocation strategy is illustrated in Fig. 8. This structure enables the vehicle to respond dynamically to uncertainties while maintaining stability and control along its planned trajectory.

In summary, combining an offline-optimized control input set with an online feedback adjustment ensures that the vehicle operates within its designated flight envelope while adapting in real time to maintain performance under challenging conditions. The corrective control input $\Delta u(t)$, requested by the attitude feedback controller, is determined through an online optimization algorithm. The design and implementation of this online optimization algorithm are central contributions of this paper, and further details on its development and operation are presented in the following section.

V. The Proposed Online Control Allocation Algorithm

In standard redistributed pseudoinverse control allocation (RPICA) approaches, the problem of limited control input authority is solved by iterating over the admissible maneuvering set (AMS) until a feasible control input command is found [20]. To do so, the algorithm typically uses the Moore–Penrose inverse. The benefit of this approach is that a solution can often be obtained in a simple way that is real-time feasible for many aerospace applications. However, in most RPICA formulations no soft constraints on the distribution of the control effort are considered, and asymmetric input or rate limits cannot be represented adequately. For the class of HGVs studied here, these aspects are particularly critical, rendering standard RPICA solutions suboptimal.

In the proposed iterative dynamic control allocation (IDCA) algorithm, a linear filter formulation, originally introduced in [22], is employed. Unlike the Moore–Penrose inverse, this approach explicitly accounts for both the current control distribution and the allocation of the previous time step as soft constraints [26]. This implicitly incorporates actuator rates into the allocation problem. The method provides an explicit solution to the following weighted least-squares problem:

$$\begin{aligned} \min_{\mathbf{u}(t) \in \mathbb{R}^m} \quad & \|\mathbf{W}_m(\mathbf{u}(t) - \mathbf{u}_s(t))\|_2^2 + \|\mathbf{W}_r(\mathbf{u}(t) - \mathbf{u}(t-T))\|_2^2 \\ \text{subject to} \quad & \mathbf{v}(t) = \mathbf{B}\mathbf{u}(t), \end{aligned} \quad (33)$$

where $\mathbf{v}(t) = \mathbf{B}\mathbf{u}_r(t) + \Delta\mathbf{v}(t)$ is the virtual control input to be generated. The desired steady-state solution $\mathbf{u}_s(t)$ is specified in Sect. V.B. The algorithm is designed so that, if $\mathbf{u}_s(t)$ is feasible, the steady-state solution converges to $\mathbf{u}_s(t)$ or to a solution close to it. The weighting matrices \mathbf{W}_m and \mathbf{W}_r are symmetric and defined as functions of the state and control; their detailed design is discussed in Sect. V.A.

Since \mathbf{W}_m and \mathbf{W}_r are symmetric, the combined weighting

$$\mathbf{W} = \sqrt{\mathbf{W}_m^2 + \mathbf{W}_r^2} \quad (34)$$

is non-singular. This allows the reformulation of Eq. (33) into the simpler criterion

$$\min_{\mathbf{u}(t) \in \mathbb{R}^m} \quad \|\mathbf{W}(\mathbf{u}(t) - \mathbf{u}_0(t))\|_2, \quad (35)$$

with

$$\mathbf{u}_0(t) = \mathbf{W}^{-2}(\mathbf{W}_m^2\mathbf{u}_s(t) + \mathbf{W}_r^2\mathbf{u}(t-T)).$$

The closed-form solution of Eq. (33), expressed in the form of Eq. (35), can be written as [22]:

$$\mathbf{u}(t) = \mathbf{E} \mathbf{u}_s(t) + \mathbf{F} \mathbf{u}(t-T) + \mathbf{G} \mathbf{v}(t), \quad (36)$$

with

$$\mathbf{E} = (\mathbf{I} - \mathbf{G}\mathbf{B})\mathbf{W}^{-2}\mathbf{W}_m^2, \quad \mathbf{F} = (\mathbf{I} - \mathbf{G}\mathbf{B})\mathbf{W}^{-2}\mathbf{W}_r^2, \quad \mathbf{G} = \mathbf{W}^{-1}(\mathbf{B}\mathbf{W}^{-1})^+.$$

The explicit solution of Eq. (36) is used within an iterative procedure to enforce actuator constraints. The algorithm is executed within a fixed controller cycle, so external variables such as $\mathbf{u}(t-T)$ and $\mathbf{x}(t)$ are treated as constant during the inner iterations. A closely related line of work was presented by Burken et al. [6], who introduced a fixed-point, quadratic-programming-based iteration scheme for control allocation. Their method shares structural similarities with the iterative procedures considered here, in that both refine the solution by re-evaluating residual commands under actuator constraints. While the fixed-point scheme demonstrated promising performance for asymmetric re-entry vehicle configurations and provided a rigorous QP-based foundation for handling magnitude constraints, actuator rate limits were only mentioned as a possible extension and not explicitly included. By contrast, the algorithm presented in the following integrates rate-dependent limits directly into the allocation problem, both as explicit constraints and as soft penalties in the weighted least-squares cost. Moreover, the proposed formulation emphasizes practical implementation by illustrating how the weighting structure can incorporate operational considerations such as thermal load reduction and drag-sensitive allocation, and by providing empirical evidence in the simulation results that the method can robustly handle strongly time-varying, state- and operating-point-dependent actuator constraints.

Figure 9 illustrates the IDCA process. The iterative procedure allows a maximum number of N iterations, with each step indexed by (j) . The actual number of iterations is denoted by $N_{\text{iter}} \leq N$. If a valid solution is found earlier, or if no further unsaturated actuators are available, the process terminates after N_{iter} iterations.

We define the iterative residual $\mathbf{v}^{(j)}$. Initially, the control input $\mathbf{u}^{(1)}$, corresponding to $\mathbf{v}^{(0)} = \mathbf{v}(t)$, is computed from Eq. (36). If $\mathbf{u}^{(1)}$ respects all actuator constraints and delivers the required virtual control, it becomes the final solution. Otherwise, the process continues.

The achieved saturated virtual control in iteration step j is

$$\mathbf{v}^{(j)} = \mathbf{B} S(\mathbf{u}^{(j)}, \dot{\mathbf{u}}^{(j)}, \mathbf{x}(t)), \quad (37)$$

where $S(\cdot)$ is the state- and rate-dependent saturation function (cf. Eq. (29)), $\dot{\mathbf{u}}^{(j)} = \frac{1}{T}(\mathbf{u}^{(j)} - \mathbf{u}_\tau)$ and $\mathbf{u}_\tau = \mathbf{u}(t-T)$ die control input of the last time step.

If actuators saturate, the corresponding columns of \mathbf{B} are set to zero, yielding the reduced matrix \mathbf{B}_s . Input limits

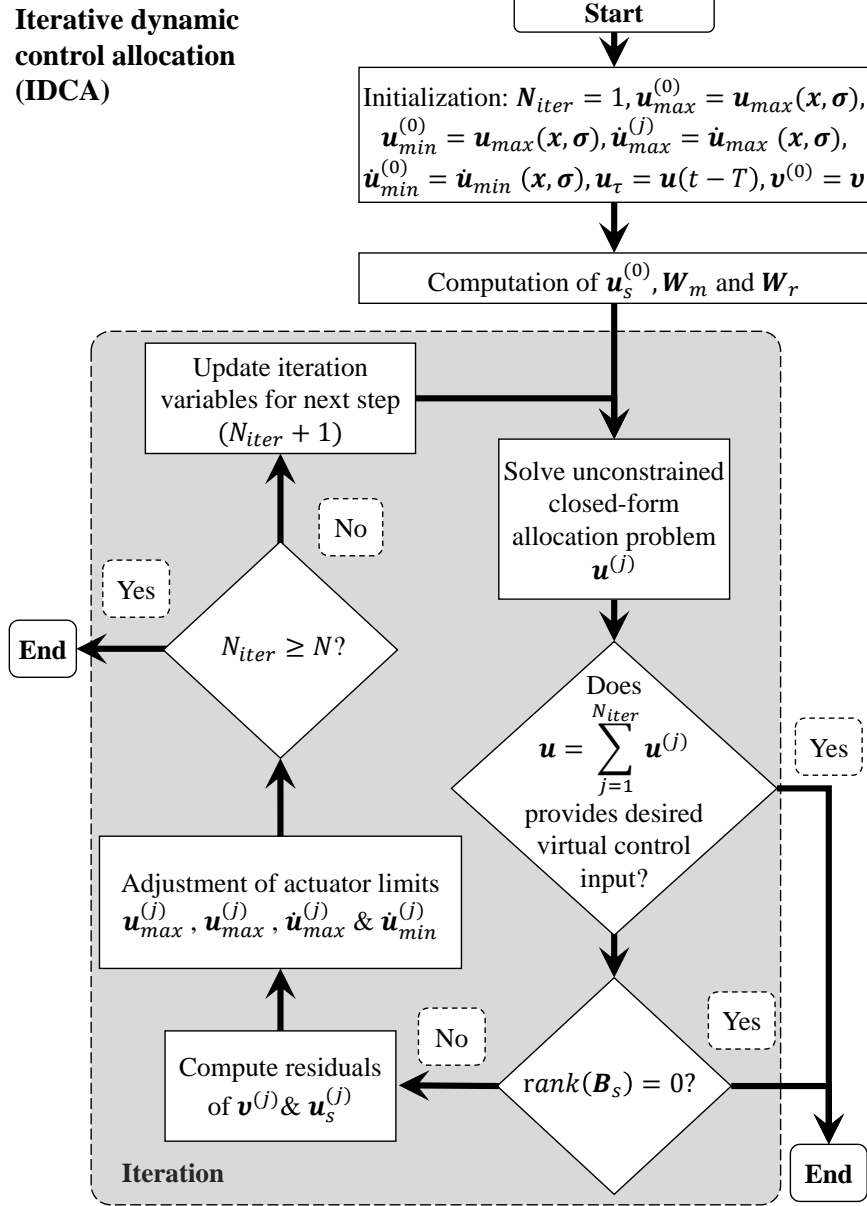


Figure 9 Flowchart of the proposed IDCA algorithm.

are updated at each step to ensure feasibility:

$$u_{\max}^{(j)} = u_{\max}^{(j-1)} - u^{(j)}, \quad u_{\min}^{(j)} = u_{\min}^{(j-1)} - u^{(j)}, \quad (38)$$

$$\dot{u}_{\max}^{(j)} = \dot{u}_{\max}^{(j-1)} - \frac{1}{T}(u^{(j)} - u_{\tau}), \quad \dot{u}_{\min}^{(j)} = \dot{u}_{\min}^{(j-1)} - \frac{1}{T}(u^{(j)} - u_{\tau}). \quad (39)$$

A corresponding adjustment of the steady-state solution u_s is also applied. The residual virtual control vector is then updated as

$$v^{(j)} = v^{(j-1)} - \mathbf{B}_s S(u^{(j)}, \dot{u}^{(j)}, x(t)). \quad (40)$$

In the next iteration, $\nu^{(j)}$ is reallocated using \mathbf{B}_s and the updated limits. The procedure continues until the required virtual control is achieved, no unsaturated actuators remain, or N is reached. The final commanded control vector is

$$\mathbf{u}(t) = \sum_{j=1}^{N_{\text{iter}}} \mathbf{u}^{(j)}. \quad (41)$$

For completeness, alongside the mathematical steps and the process visualization in Fig. 9, the algorithm is also summarized in pseudocode to complement the formulation and facilitate implementation.

Algorithm 1 Iterative Dynamic Control Allocation (IDCA)

```

1: Initialize:  $N_{\text{iter}} \leftarrow 1$ ,  $\mathbf{u}_{\max}^{(0)} \leftarrow \mathbf{u}_{\max}(\mathbf{x}, \boldsymbol{\sigma})$ ,  $\mathbf{u}_{\min}^{(0)} \leftarrow \mathbf{u}_{\min}(\mathbf{x}, \boldsymbol{\sigma})$ ,  $\dot{\mathbf{u}}_{\max}^{(0)} \leftarrow \dot{\mathbf{u}}_{\max}(\mathbf{x}, \boldsymbol{\sigma})$ ,  $\dot{\mathbf{u}}_{\min}^{(0)} \leftarrow \dot{\mathbf{u}}_{\min}(\mathbf{x}, \boldsymbol{\sigma})$ ,  $\mathbf{u}_\tau \leftarrow \mathbf{u}(t - T)$ ,  $\mathbf{u}_s^{(0)} \leftarrow \mathbf{u}_s$ ,  $\nu^{(0)} \leftarrow \nu$ 
2: Compute  $\mathbf{u}_s^{(0)}$ ,  $\mathbf{W}_m$ ,  $\mathbf{W}_r$ 
3: while  $N_{\text{iter}} < N$  do
4:   Compute candidate input  $\mathbf{u}^{(j)}$ 
5:   if  $\mathbf{u} = \sum_{j=1}^{N_{\text{iter}}} \mathbf{u}^{(j)}$  delivers desired  $\nu$  then
6:     Terminate with:  $\mathbf{u}(t) = \sum_{j=1}^{N_{\text{iter}}} \mathbf{u}^{(j)}$ 
7:   end if
8:   Compute residuals of  $\nu^{(j)}$  and  $\mathbf{u}_s^{(j)}$ 
9:   if  $\text{rank}(\mathbf{B}_s) = 0$  then
10:    Terminate with:  $\mathbf{u}(t) = \sum_{j=1}^{N_{\text{iter}}} \mathbf{u}^{(j)}$ 
11:   end if
12:   Update actuator limits  $\mathbf{u}_{\max}^{(j)}$ ,  $\mathbf{u}_{\min}^{(j)}$ ,  $\dot{\mathbf{u}}_{\max}^{(j)}$ ,  $\dot{\mathbf{u}}_{\min}^{(j)}$ 
13:   Update iteration counter  $N_{\text{iter}} \leftarrow N_{\text{iter}} + 1$ 
14: end while
15: Output: final control input  $\mathbf{u}(t)$ 

```

A. Control Input-Based Weighting Matrices

The main motivation of the here proposed iterative control allocation approach is to consider soft constraints on the distribution of the control efforts. To do so, a meaningful design of the weighting matrices $\mathbf{W}_m(\mathbf{x}, \mathbf{u})$ and $\mathbf{W}_r(\dot{\mathbf{u}})$ is leveraged. The magnitude weighting matrix $\mathbf{W}_m(\mathbf{x}, \mathbf{u})$ is designed to allocate weights to control effectors based on their current measured deflection state u_i , as well as to use the weighting to prioritize control surfaces with less thermal loads acting on them. The overall matrix $\mathbf{W}_m(\mathbf{x}(t), \mathbf{u}(t))$ is defined as:

$$\mathbf{W}_m = \begin{bmatrix} w_{m,1} & 0 & 0 & 0 \\ 0 & w_{m,2} & 0 & 0 \\ 0 & 0 & w_{m,3} & 0 \\ 0 & 0 & 0 & w_{m,4} \end{bmatrix} + \epsilon \mathbf{I}, \quad (42)$$

with $\epsilon \in \mathbb{R}_{>0}$ being a small positive scalar and \mathbf{I} a square identity matrix used to prevent the loss of needed symmetric matrix properties in the case that one or more weight elements goes to zero. The elements $w_{m,i}(\mathbf{x}(t), u_i(t))$ represent, for each control surface i , a multiplicative weighting function designed to balance the two considered soft constraints in the allocation, as follows:

$$w_{m,i} = \underbrace{w_{m_D,i}(u_i(t))}_{\substack{\text{Weighting function} \\ \text{for deflection magnitude}}} \cdot \underbrace{w_{m_T,i}(\mathbf{x}(t), \boldsymbol{\sigma}(t))}_{\substack{\text{Weighting function} \\ \text{for thermal loads}}}, \quad (43)$$

with $w_{m_D,i}(u_i(t))$ being the weighting function for the deflection magnitude and $w_{m_T,i}(\mathbf{x}(t), \boldsymbol{\sigma}(t))$ being the weighting function to address the effects of thermal loads for each effector i . The weighting function $w_{m_D,i}(u_i(t))$ is defined as:

$$w_{m_D,i}(u_i(t)) = \frac{u_i(t)}{u_{\max,i}(\mathbf{x}(t), \boldsymbol{\sigma}(t))}. \quad (44)$$

This formulation assigns higher weights to effectors with larger deflection states, reflecting a strategic preference to distribute control efforts equally among available actuators. This approach has the operational benefit of reducing the tendency for each actuator to reach saturation.

To define $w_{m_T,i}(\mathbf{x}(t))$ in a computationally efficient manner, we utilized insights from wind tunnel experiments conducted at the DLR Institute of Aerodynamics and Flow Technology [27]. Figure 10 shows an image of the wind tunnel test of the GHGV-2 at Mach 8.7, angle of attack $\alpha = 10^\circ$, and sideslip angle $\beta = 0^\circ$, with all flaps deflected by 20° .

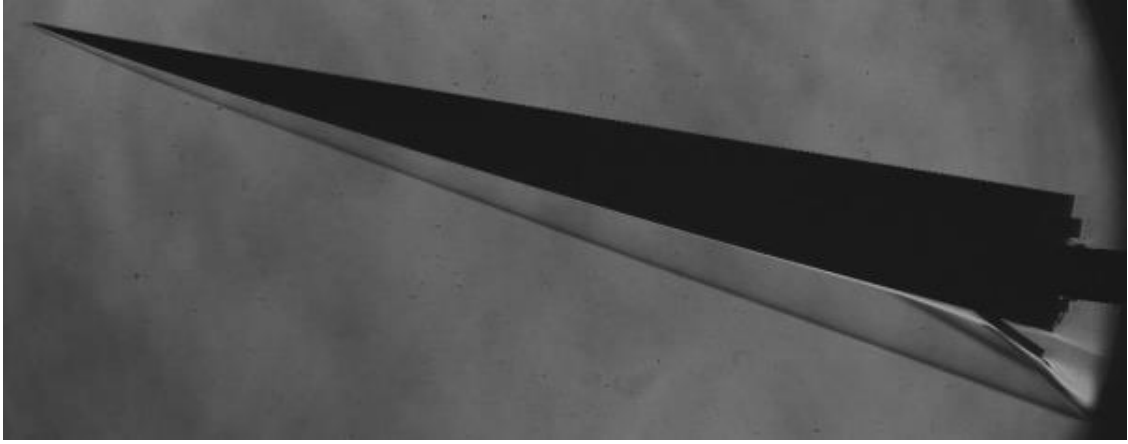


Figure 10 Wind tunnel test of GHGV-2 with $M = 8.7$, $\alpha = 10^\circ$, and $\beta = 0^\circ$; all flaps deflected by 20° [27].

The obtained results demonstrated that during endoatmospheric flight at high Mach numbers, thermal loads on the vehicle's lower side are more critical than the upper side due to increased heat flux. This phenomenon is attributed to the vehicle's operation at predominantly positive angles of attack, which alters the aerodynamic heating distribution and

results in less severe thermal conditions on the upper part of the vehicle. Therefore, it is preferable to utilize the upper flaps as much as possible during the mission while minimizing deflection of the lower flaps. The results also confirmed that thermal loads on the flaps increase with deflection angle for both upper and lower control surfaces. It is important to note that this distribution of thermal loads between upper and lower surfaces depends on the angle of attack: at positive angles of attack, the lower flaps experience higher thermal loads, whereas at negative angles of attack, the upper flaps are more critically affected. Similarly, sideslip angles can cause imbalances between the left and right sides of the vehicle.

Given the complex nature of thermal modeling, directly incorporating heat flux considerations into the computation of $w_{mT,i}(\mathbf{x}(t))$ was deemed impractical. However, in all relevant cases, we observed a strong positive correlation between aerodynamic drag and heat flux with increasing control deflection angles across all control surfaces. The extent of this correlation varies depending on effector position. This correlation allows us to use aerodynamic drag as a proxy for thermal loads in the weighting function. Assuming these influences can be approximated as affine, the thermal weighting for control surfaces is computed as:

$$w_{mT,i}(\mathbf{x}(t), \boldsymbol{\sigma}(t)) = \frac{C_{D,u_i}(\mathbf{x}(t))}{\max\{C_{D,u_1}(\mathbf{x}(t), \boldsymbol{\sigma}(t)), \dots, C_{D,u_m}(\mathbf{x}(t), \boldsymbol{\sigma}(t))\}}, \quad (45)$$

where the denominator represents the maximum state-dependent aerodynamic drag coefficient among all control surfaces, and $C_{D,u_i}(\mathbf{x}(t), \boldsymbol{\sigma}(t))$ is the aerodynamic drag coefficient of control surface i . This formulation assigns higher weights to surfaces with higher drag contributions, thereby favoring allocation to surfaces with reduced thermal loads.

The rate weighting matrix $\mathbf{W}_r(\dot{\mathbf{u}}(t - T))$, designed to address the dynamic aspects of the control allocation problem by considering the rates of deflection, is defined as:

$$\mathbf{W}_r = \begin{bmatrix} w_{r,1} & 0 & 0 & 0 \\ 0 & w_{r,2} & 0 & 0 \\ 0 & 0 & w_{r,3} & 0 \\ 0 & 0 & 0 & w_{r,4} \end{bmatrix} + \epsilon \mathbf{I}, \quad (46)$$

where $w_{r,i}(\dot{u}_i(t - T))$ represents, for each control surface i , a rate-dependent weighting function defined as

$$w_{r,i} = \frac{|\dot{u}_i(t - T)|}{\dot{u}_{\text{crit},i}(\mathbf{x}(t), \boldsymbol{\sigma}(t))}, \quad (47)$$

with the actuator rate at the initial time, when the allocation algorithm starts, given by

$$\dot{u}_i(t-T) = \frac{1}{T}(u_i(t-T) - u_i(t-2T)). \quad (48)$$

The critical rate limit $\dot{u}_{\text{crit},i}(\mathbf{x}(t))$, representing the rate bound the actuator is approaching, is defined as:

$$\dot{u}_{\text{crit},i}(\mathbf{x}(t)) = \begin{cases} |\dot{u}_{\text{max},i}(\mathbf{x}(t), \sigma(t))|, & \dot{u}_i(t-T) \geq 0, \\ |\dot{u}_{\text{min},i}(\mathbf{x}(t), \sigma(t))|, & \dot{u}_i(t-T) < 0. \end{cases} \quad (49)$$

The carefully crafted weighting matrices \mathbf{W}_m and \mathbf{W}_r contribute to the proposed control allocation algorithm's overall efficiency and stability, aligning with the discussed operational objectives. However, it is important to note that the proposed weighting functions $w_{m,i}(\mathbf{x}(t), u_i(t))$ and $w_{r,i}(\dot{u}_i(t-T))$ establish linear relationships with respect to the maximum and minimum values $u_{\text{max},i}(\mathbf{x}(t))$, $u_{\text{min},i}(\mathbf{x}(t))$, $\dot{u}_{\text{max},i}(\mathbf{x}(t))$, and $\dot{u}_{\text{min},i}(\mathbf{x}(t))$. Similarly, they assume an affine correlation between aerodynamic drag and thermal loads. While this linear approach ensures computational simplicity and efficiency, it inherently represents an idealized approximation. The proposed methodology simplifies the weighting function design but may not fully capture the nonlinear dependencies observed in practice. Future work could investigate incorporating nonlinear weighting schemes to better account for the interactions between deflection states, aerodynamic drag, and thermal effects while maintaining computational feasibility.

B. Designer Preference-Based Steady State Solution

The proposed IDCA approach allows it to consider a desired steady-state control input vector $\mathbf{u}_s(t)$. This section discusses how a good guess for $\mathbf{u}_s(t)$ is obtained based on an a priori known baseline control input $\mathbf{u}_r(t)$ and designer preferences in the control effector usage of the hypersonic glide vehicle. Even though the computed $\mathbf{u}_s(t)$ might not always provide a perfect solution to the requested virtual control command or in some cases might not be physically feasible under certain constraints, it serves as a desirable reference point or target for the redistributed control allocation algorithm. As discussed in Sect. IV, in a scenario where no external disturbances or model uncertainties are present, the baseline control input $\mathbf{u}_r(t)$ would be sufficient to maintain the HGV on its reference trajectory. However, given the inherent uncertainties and potential disturbances in hypersonic flight, the control system also requires an attitude feedback controller to provide additional corrections. This controller computes a virtual control adjustment $\Delta\mathbf{u}(t)$, which compensates for deviations from the nominal trajectory. Assuming an affine nature for the control input, the desired steady state control input can be computed as:

$$\mathbf{u}_s(t) = \mathbf{u}_r(t) + \Delta\mathbf{u}(t), \quad (50)$$

where $\Delta\mathbf{u}(t)$ represents the correction determined through the proposed online control allocation algorithm. The control input $\Delta\mathbf{u}(t)$ is generated using the following request-dependent pseudoinverse-based approach:

$$\Delta\mathbf{u}(t) = \begin{bmatrix} \Delta u_1(t) \\ \Delta u_2(t) \\ \Delta u_3(t) \\ \Delta u_4(t) \end{bmatrix} = \mathbf{B}_C^\dagger(\Delta\mathbf{v}(t)) \Delta\mathbf{v}(t), \quad \text{with} \quad \mathbf{B}_C(\Delta\mathbf{v}(t)) = \begin{bmatrix} \mathbf{B}_{\nu_x}(\Delta\nu_x(t)) \\ \mathbf{B}_{\nu_y}(\Delta\nu_y(t)) \\ \mathbf{B}_{\nu_z}(\Delta\nu_z(t)) \end{bmatrix}. \quad (51)$$

Here $\mathbf{B}_C(\Delta\mathbf{v}(t))$ represents a conditionalized control effectiveness matrix. The submatrices $\mathbf{B}_{\nu_x}(\Delta\nu_x(t))$, $\mathbf{B}_{\nu_y}(\Delta\nu_y(t))$, and $\mathbf{B}_{\nu_z}(\Delta\nu_z(t))$ correspond to the three virtual control channels. The requested corrective virtual control command vector is

$$\Delta\mathbf{v}(t) = [\Delta\nu_x(t), \Delta\nu_y(t), \Delta\nu_z(t)]^T,$$

which provides information about the required virtual control moments along the body axes.* Based on flight dynamical properties and engineering preferences, certain elements of $\mathbf{B}_{\nu_x}(\Delta\nu_x(t))$, $\mathbf{B}_{\nu_y}(\Delta\nu_y(t))$, and $\mathbf{B}_{\nu_z}(\Delta\nu_z(t))$ are sparsified to force an allocation on desired control effectors.

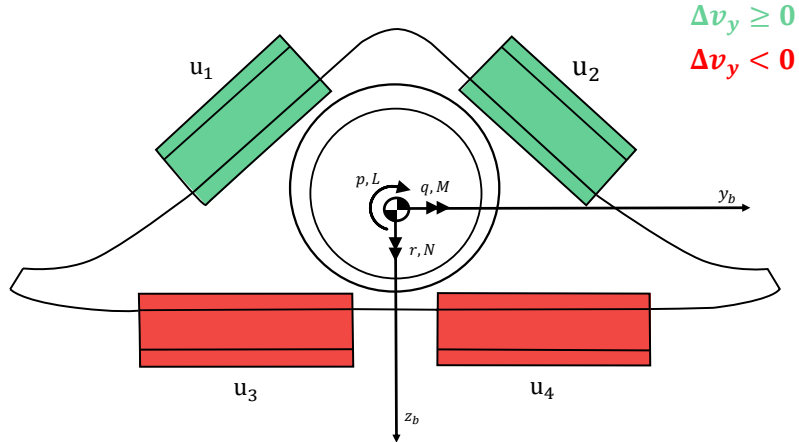


Figure 11 Corresponding control surface selection for positive and negative incremental pitch moment $\Delta\nu_y$ commands.

Fig. 11 illustrates how the appropriate control surfaces are identified for an example of a virtual pitch command $\Delta\nu_y(t)$. For a positive pitch command $\Delta\nu_y(t) > 0$, both the upper flaps u_1 and u_2 are identified as appropriate. Conversely, for a negative pitch command $\Delta\nu_y(t) < 0$, u_3 and u_4 make the most sense from a flight dynamical

*The abstract virtual controls ν_x, ν_y, ν_z correspond to the physical roll, pitch, and yaw moments L, M, N in the body-fixed frame. We retain the abstract notation here to emphasize the generality of the formulation.

perspective. This leads to the following sign-based conditionalization of $\mathbf{B}_{\nu_y}(\Delta\nu_y(t))$ in the pitch-related row:

$$\mathbf{B}_{\nu_y}(\Delta\nu_y(t)) = \begin{cases} \begin{pmatrix} \frac{\partial\nu_y}{\partial u_1} & \frac{\partial\nu_y}{\partial u_2} & 0 & 0 \end{pmatrix} & \text{if } \Delta\nu_y(t) \geq 0, \\ \begin{pmatrix} 0 & 0 & \frac{\partial\nu_y}{\partial u_3} & \frac{\partial\nu_y}{\partial u_4} \end{pmatrix} & \text{if } \Delta\nu_y(t) < 0. \end{cases} \quad (52)$$

A similar approach is taken for the roll component $\Delta\nu_x(t)$ and the yaw component $\Delta\nu_z(t)$. The roll component $\mathbf{B}_{\nu_x}(\Delta\nu_x(t))$ is conditionalized in the following way:

$$\mathbf{B}_{\nu_x}(\Delta\nu_x(t)) = \begin{cases} \begin{pmatrix} 0 & \frac{\partial\nu_x}{\partial u_2} & \frac{\partial\nu_x}{\partial u_3} & 0 \end{pmatrix} & \text{if } \Delta\nu_x(t) \geq 0, \\ \begin{pmatrix} \frac{\partial\nu_x}{\partial u_1} & 0 & 0 & \frac{\partial\nu_x}{\partial u_4} \end{pmatrix} & \text{if } \Delta\nu_x(t) < 0. \end{cases} \quad (53)$$

The yaw-related row $\mathbf{B}_{\nu_z}(\Delta\nu_z(t))$ is defined as:

$$\mathbf{B}_{\nu_z}(\Delta\nu_z(t)) = \begin{cases} \begin{pmatrix} 0 & \frac{\partial\nu_z}{\partial u_2} & 0 & \frac{\partial\nu_z}{\partial u_4} \end{pmatrix} & \text{if } \Delta\nu_z(t) \geq 0, \\ \begin{pmatrix} \frac{\partial\nu_z}{\partial u_1} & 0 & \frac{\partial\nu_z}{\partial u_3} & 0 \end{pmatrix} & \text{if } \Delta\nu_z(t) < 0. \end{cases} \quad (54)$$

This approach yields a reasonable and operationally desired steady state, considering factors such as actuator use, drag reduction, and thermal load minimization. If $\mathbf{u}_s(t)$ is unfeasible or not a solution to $\nu(t) = \mathbf{B}\mathbf{u}(t)$, the proposed redistributed approach will iterate to search for a viable solution close to $\mathbf{u}_s(t)$.

VI. Simulation Results

A simulation-based analysis was carried out to examine the proposed IDCA algorithm. The flight dynamics model and the applied aerodynamic data set used for the time simulations are provided in a MATLAB/Simulink environment developed for the control design of hypersonic flight vehicles; see [8] for more details.

A. Comparison analysis on static moment commands

As discussed in Sect. II.A, the presented PICA and RPICA algorithms are not necessarily capable of handling asymmetrical control input limitations. To illustrate this limitation, a simplified example of a constrained control allocation problem is considered and visualized in Fig. 12. The setup involves two control inputs $\mathbf{u} = [u_1, u_2]^T$, where the admissible set is bounded by asymmetrical magnitude constraints $\mathbf{u}_{\min} = [0, 0]^T$ and $\mathbf{u}_{\max} = [1.5, 1.5]^T$. In this stationary example, rate constraints are neglected. The control effectiveness matrix is defined as $\mathbf{B} = [0.5, -0.5]$, and

the demanded virtual control input is given by $v = 0.5$.

The set of all solutions to $v = \mathbf{B}\mathbf{u}$ forms a straight line in the (u_1, u_2) -plane, shown as the dashed black line in Fig. 12. The admissible region for \mathbf{u} is marked by the dashed red box, representing the input bounds. Thus, the set of feasible solutions corresponds to the intersection between this line and the red box. Geometrically, every point on the black line segment that lies inside the red box is a feasible solution. Among these, the optimal solution is defined as the feasible point that minimizes the cost $J = \|\mathbf{u}\|_2^2$, which corresponds to the point closest to the origin. In this case, the unique optimal solution is $\mathbf{u} = [1, 0]^T$.

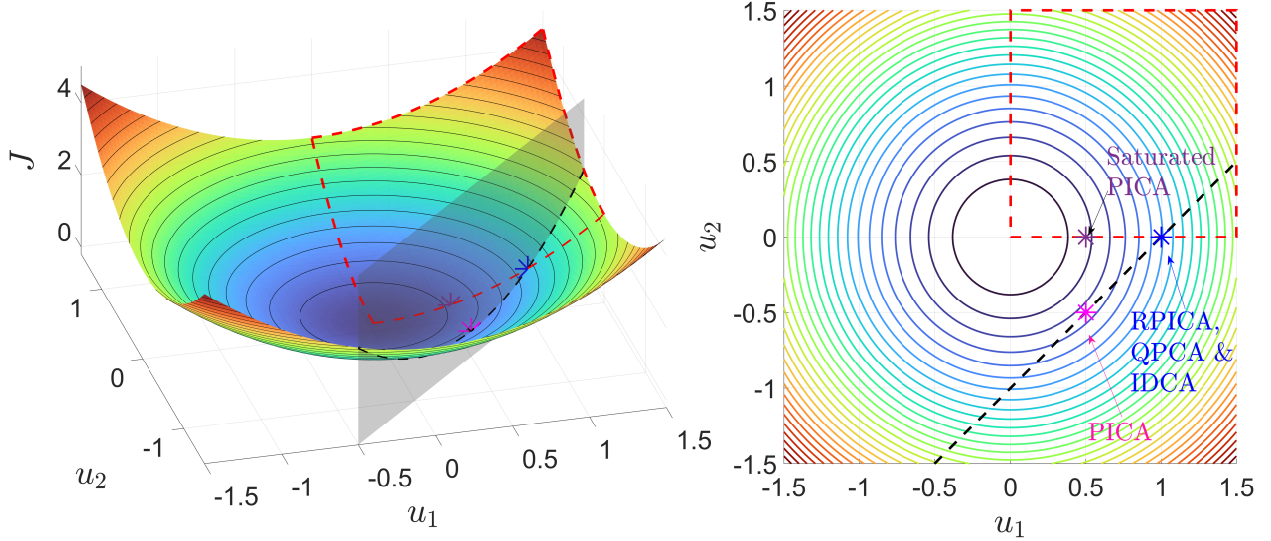


Figure 12 Results of a simple constrained control allocation problem with two inputs and asymmetrical magnitude limits.

As shown in the figure, the standard PICA algorithm computes the solution $\mathbf{u} = [0.5, -0.5]^T$ (magenta star), which satisfies the equation $v = \mathbf{B}\mathbf{u}$ but lies outside the admissible region and is therefore physically not feasible. After saturation, the corrected control input becomes $\mathbf{u} = [0.5, 0]^T$ (violet star). This input is admissible but no longer reproduces the commanded virtual input, resulting in a large allocation error. By contrast, RPICA, QPCA, and the proposed IDCA algorithm are capable of incorporating the input limits directly and compute the admissible and optimal solution $\mathbf{u} = [1, 0]^T$ (blue star). While RPICA is sufficient in this simple case, its performance deteriorates for higher-dimensional actuator systems with strong asymmetrical limits as present in the GHGV-2. QPCA is generally robust but computationally expensive, motivating the proposed IDCA algorithm that retains real-time feasibility while achieving comparable accuracy.

Based on this simple analysis, the algorithms are next evaluated at a representative operating point of the GHGV-2. The vehicle is trimmed for flight at Mach 8 and an altitude of 30 km, where the four aerodynamic control surfaces of the

HGV u_1 to u_4 are available. The admissible bounds are defined as

$$\mathbf{u}_{\min} = \begin{bmatrix} 0^\circ & 0^\circ & 0^\circ & 0^\circ \end{bmatrix}^T, \quad \mathbf{u}_{\max} = \begin{bmatrix} 20^\circ & 20^\circ & 20^\circ & 20^\circ \end{bmatrix}^T,$$

and the control effectiveness matrix at this operating point is

$$\mathbf{B} = \begin{pmatrix} -20.01 & 20.01 & 93.94 & -93.94 \\ 126.7 & 126.7 & -501.4 & -501.4 \\ -127.5 & 127.5 & -45.72 & 46.72 \end{pmatrix}. \quad (55)$$

A stationary virtual control command $\mathbf{v} = [-400, 800, -2000]^T$ Nm is prescribed, which lies within the AMS and is therefore physically realizable without violating the actuator magnitude limits. Since the command is stationary, rate constraints are not considered in this case.

The results are shown in Fig. 13. PICA generates a solution that formally satisfies the allocation equation but violates the lower input bounds for several surfaces, making it physically infeasible. Saturated PICA respects the limits but concentrates almost the entire effort on u_1 , failing to reproduce the commanded moment. RPICA also respects the bounds but suffers from premature saturation in three surfaces during the first iteration, leaving only u_1 to carry the residual, which again results in a large allocation error. In contrast, QPCA and IDCA both provide admissible deflections that satisfy the command. Their allocations are nearly identical, with QPCA solving a quadratic optimization problem and IDCA iterating dynamically over weighted residuals.

Table 3 Results for the GHGV-2 stationary allocation case.

Method	Cost $J = \ \mathbf{u}\ _2$ [Nm]	Error norm $\ \mathbf{v} - \mathbf{Bu}\ _2$ [Nm]	Computation time [s]
PICA	11.3749	1.3270×10^{-12}	1.5760×10^{-4}
Saturated PICA	8.1773	1.0140×10^3	1.5760×10^{-4}
RPICA	14.1015	1.0140×10^3	3.9210×10^{-4}
QPCA	16.1473	2.2737×10^{-13}	0.3911
IDCA	16.2146	3.2155×10^{-13}	5.5550×10^{-4}

Table 3 provides the allocation cost $J = \|\mathbf{u}\|_2$, the allocation error $\|\mathbf{v} - \mathbf{Bu}\|_2$, and the computation time. PICA exhibits the lowest cost but yields an invalid solution, while saturated PICA and RPICA produce high allocation errors despite respecting the bounds. QPCA and IDCA achieve nearly identical, minimal error norms, but QPCA requires several orders of magnitude longer computation time. IDCA achieves the same level of accuracy at real-time-capable runtimes, only marginally slower than PICA and RPICA.

To further assess robustness, a Monte Carlo analysis with $N = 1000$ random virtual control commands is conducted.

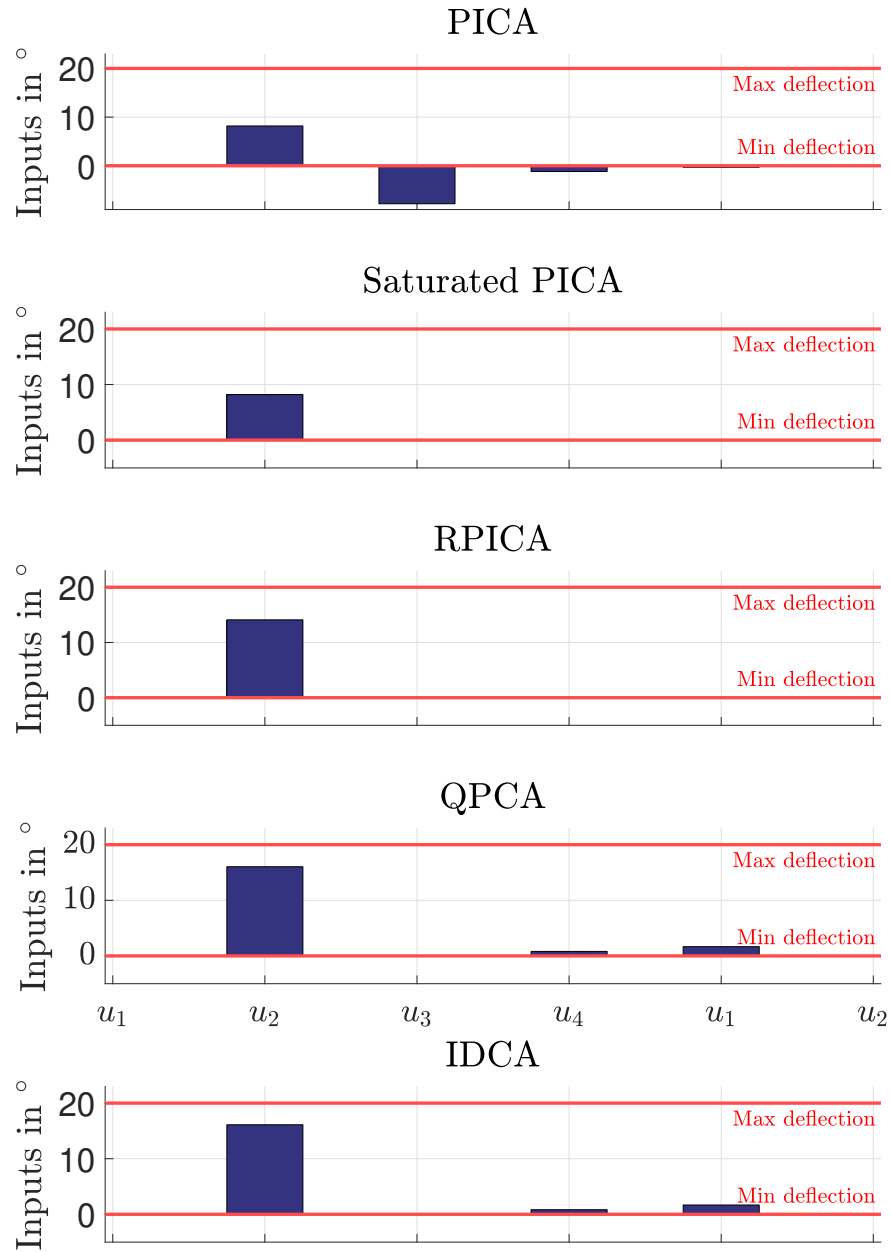


Figure 13 Obtained control deflections for different allocation algorithms under a moment command within the AMS of the GHGV-2.

The mean command vector is chosen as $\nu_m = [-100, 300, -500]^T$, with each component modeled as a Gaussian random variable $\nu_i \sim \mathcal{N}(\nu_{m,i}, \sigma_i^2)$. The standard deviations are set to $\sigma_i = \frac{2}{3}|\nu_{m,i}|$ for $i = 1, 2, 3$, such that the $\pm 3\sigma$ range spans approximately twice the mean value of each component. Random commands are then generated according to $\nu = \nu_m + \sigma \odot \mathbf{z}$, where \mathbf{z} is a vector of independent standard normal variables and \odot denotes element-wise multiplication. A total of $N = 1000$ such samples is generated, ensuring a broad coverage of possible commands both near and within the AMS. The actuator limits and the control effectiveness matrix remain unchanged from the stationary case.

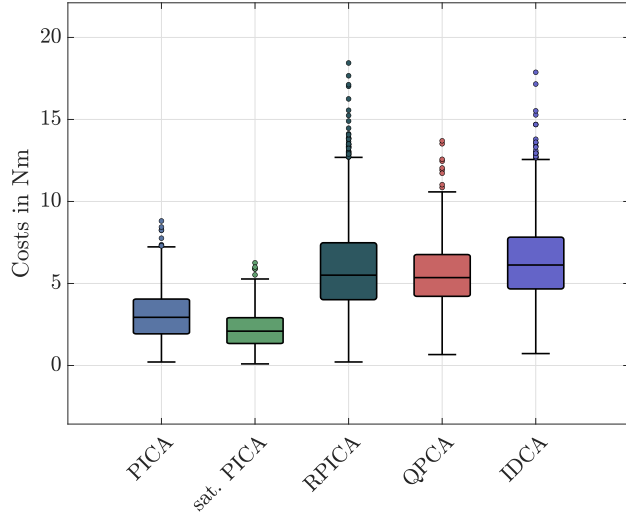


Figure 14 Distribution of allocation costs $J = \|\mathbf{u}\|_2$ over $N = 1000$ Monte Carlo samples.

Figure 14 shows the cost distributions. IDCA produces slightly higher costs than QPCA and RPICA on average, but all results remain within physically reasonable ranges. PICA frequently exhibits lower costs, though many of its solutions are inadmissible.

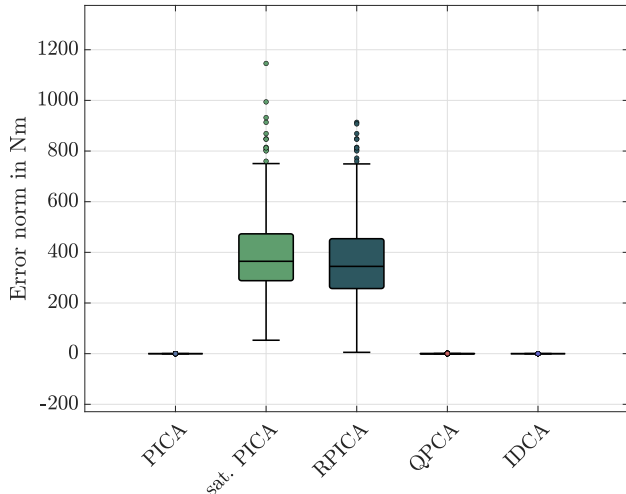


Figure 15 Distribution of allocation error $\|\nu - \mathbf{B}\mathbf{u}\|_2$ over $N = 1000$ Monte Carlo samples.

The corresponding allocation error distributions in Fig. 15 reveal that PICA, QPCA, and IDCA achieve consistently low errors, whereas saturated PICA and RPICA produce significantly larger errors, often exceeding several hundred Nm. This confirms that PICA neglects input limits, while QPCA and IDCA generate realizable allocations.

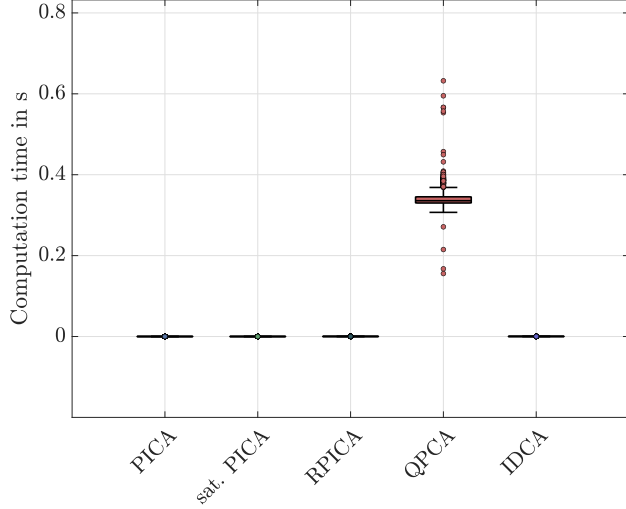


Figure 16 Computation times across $N = 1000$ Monte Carlo samples.

Finally, Fig. 16 compares computation times. QPCA requires orders of magnitude longer runtimes due to solving a quadratic program at every iteration, while PICA, saturated PICA, and RPICA remain computationally fast but unreliable. IDCA achieves runtimes in the millisecond range, slightly above RPICA, but still compatible with real-time requirements.

Overall, the stationary and Monte Carlo analyses confirm that while PICA produces formally correct but inadmissible solutions, and RPICA respects constraints but distributes residuals poorly, QPCA and IDCA achieve accurate, realizable allocations. The decisive advantage of IDCA is that it matches the accuracy of QPCA at real-time-capable runtimes, demonstrating its suitability for onboard implementation in the GHGV-2.

B. Time-varying moment commands on proposed algorithm

For this assessment, the same control effectiveness matrix \mathbf{B} as in Eq. (55) is considered. The GHGV-2 is again trimmed at Mach 8 and an altitude of 30 km, representing the same operating condition as before. In this analysis, however, the magnitude limits of the control surfaces are modeled as time-varying functions in order to capture the dynamic effects of varying aerodynamic loads at high Mach numbers. It is assumed that the influence of dynamic pressure leads to a reduction in the achievable upper magnitude bound of the actuators, while the lower magnitude bound remains at zero for all control surfaces, as it is not significantly affected by external influences due to the direction

of the resulting aerodynamic forces. To model this effect, the upper bounds are expressed as a sinusoidal modulation:

$$u_{\max}(t) = u_{\max,\text{full}} \cos(\Lambda(t)),$$

where $u_{\max,\text{full}} = 20^\circ$ denotes the technically achievable maximum flap deflection and $\Lambda(t)$ is a freely chosen modulation function.

In addition to time-varying magnitude bounds, rate constraints are considered as well. The upper and lower bounds of the rates, $|\dot{u}_{\max}|$ and $|\dot{u}_{\min}|$, are modeled as time-dependent functions. The upper rate limit decreases from $20^\circ/\text{s}$ to $10^\circ/\text{s}$ over the simulation, reflecting the reduced ability of actuators to achieve high positive rates under increasing aerodynamic loads. Conversely, the lower rate limit is assumed to increase from $-20^\circ/\text{s}$ to $-30^\circ/\text{s}$, because the aerodynamic forces facilitate the retraction of the control surfaces. This asymmetry captures the physical reality that positive rate changes become more restricted, while negative rate changes become easier to achieve as the flight condition evolves.

The allocation module is tested with a sinusoidal virtual control input command $\mathbf{v}(t) = [v_x(t), v_y(t), v_z(t)]^T$. The chosen command alternates between feasible and infeasible values with respect to the AMS, enabling an evaluation of the algorithm's performance under both realizable and saturated conditions. Figure 17 compares the commanded virtual control inputs (green) with the moments generated by the IDCA algorithm (blue). A generally close tracking is observed, particularly for v_z , while noticeable deviations appear in v_x and v_y whenever actuator magnitude or rate saturation is encountered. During unsaturated phases the algorithm achieves high accuracy, with nearly perfect matching of the requested commands.

Figure 18 shows the error between the requested and generated commands, defined as

$$\Delta\mathbf{v}(t) = \mathbf{v}(t) - \mathbf{B}\mathbf{u}(t).$$

The results confirm that the error converges towards zero in non-saturated phases, while in saturated regimes distinct deviations occur. The error magnitudes align with the observations from Fig. 17, where v_y exhibits the largest deviations during phases of strong demand. This correlation indicates that actuator constraints directly determine the achievable accuracy of the allocation.

The actuator magnitudes u_1, \dots, u_4 and their time-varying bounds are shown in Fig. 19. The trajectories clearly demonstrate that all commands remain within the admissible set. In the initial phase, a nearly linear increase is visible for u_1 and u_2 , which indicates active rate saturation: since the maximum rate is reached, the magnitude grows linearly until the limit changes. Comparing with Fig. 20 confirms this behavior, as \dot{u}_1 and \dot{u}_2 remain pinned at their respective limits during these phases. The corresponding deviations in Δv_x and Δv_y highlight the direct causal link between

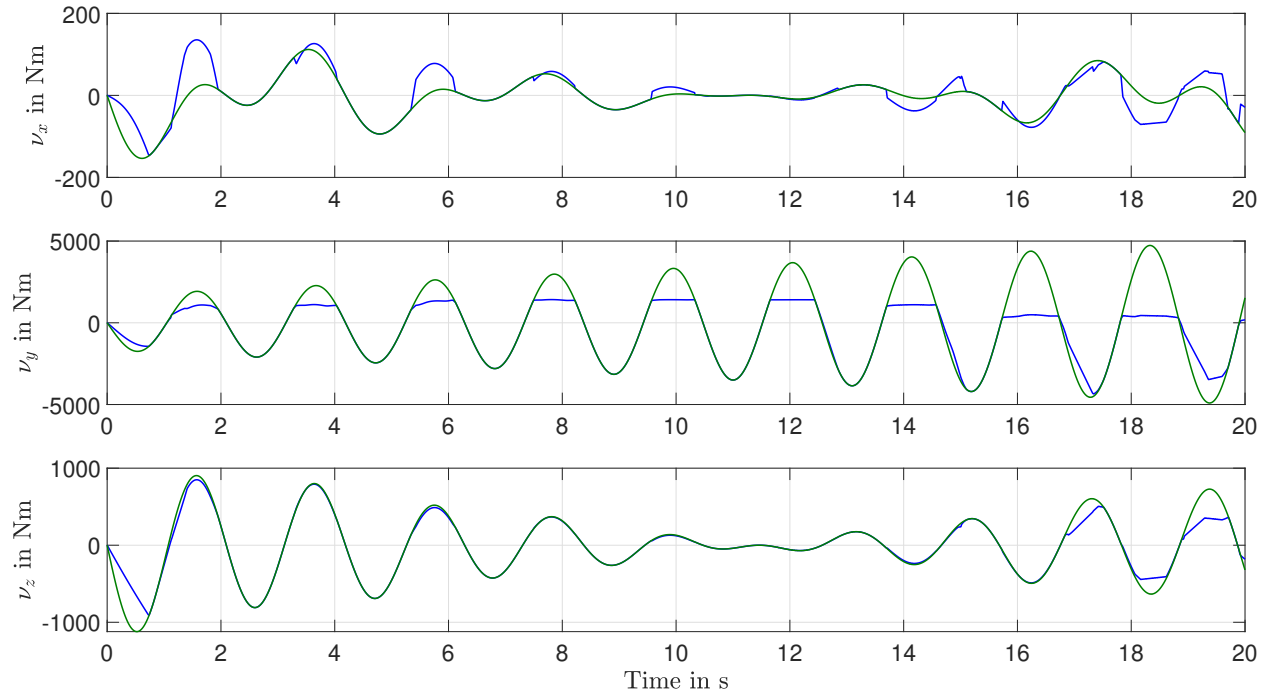


Figure 17 Results for the virtual control commands ν_x , ν_y , and ν_z . Green: commanded input. Blue: generated input after allocation.

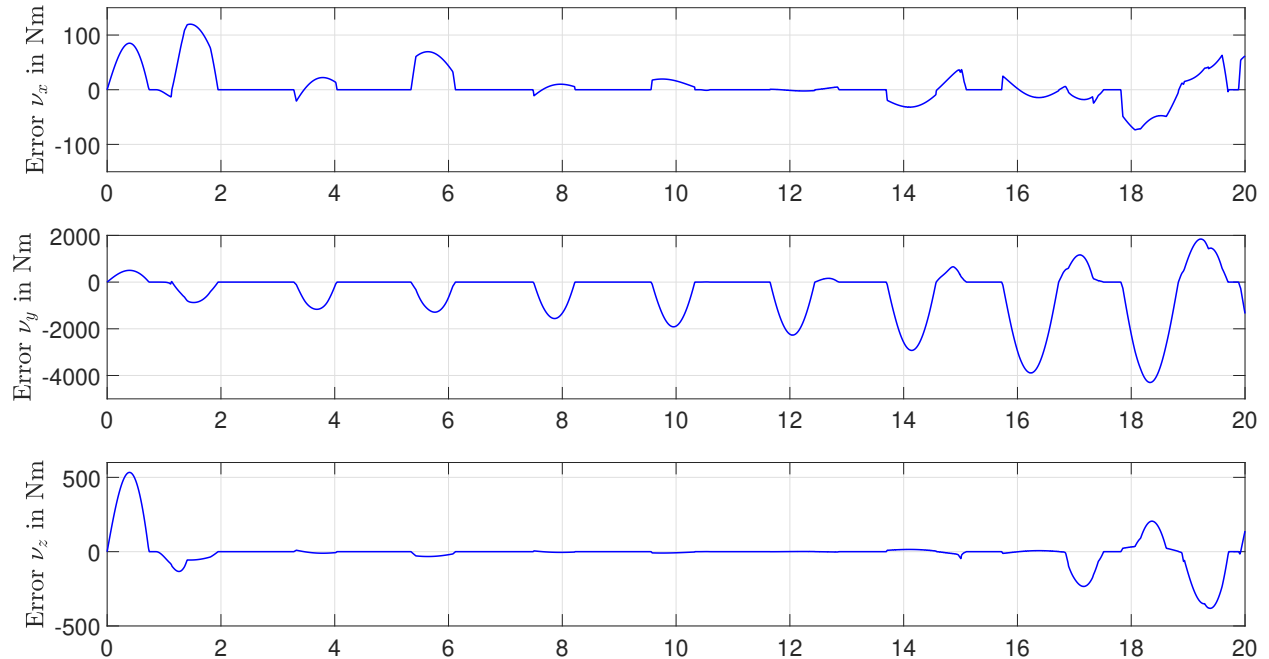


Figure 18 Error between commanded and generated virtual control inputs ν_x , ν_y , and ν_z . Blue lines: allocation error time series.

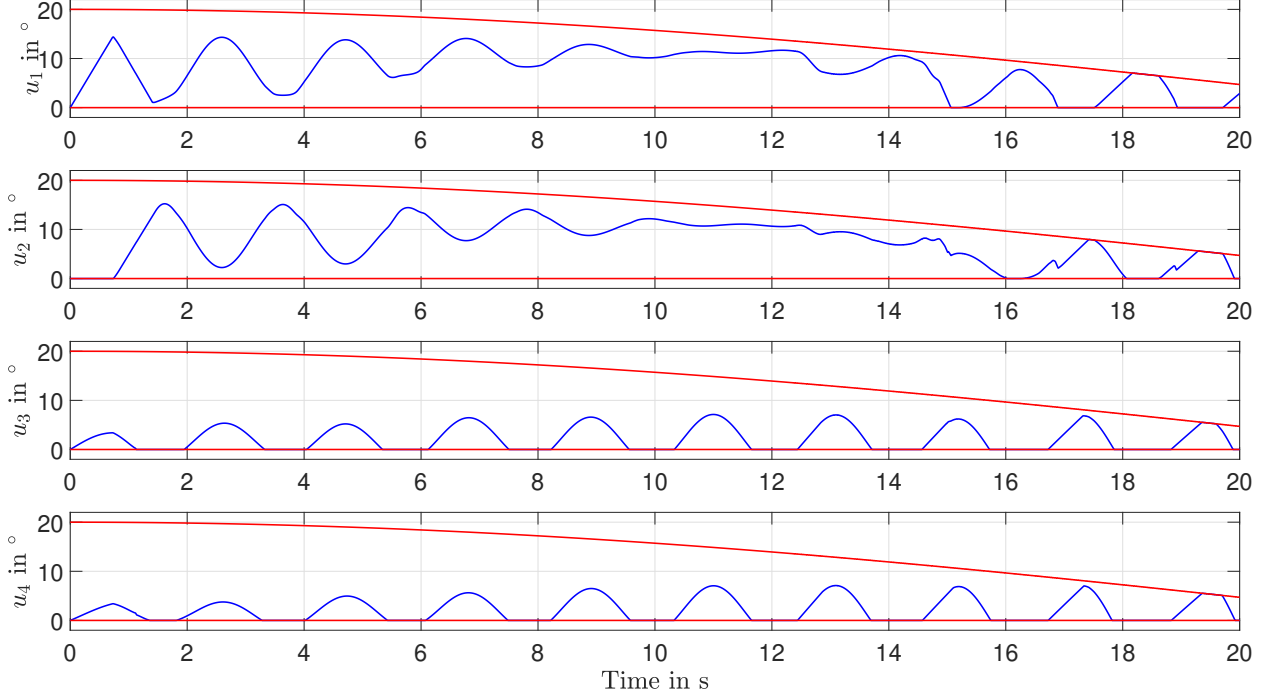


Figure 19 Computed control input magnitudes with time-varying magnitude constraints. Blue: generated deflections. Red: admissible bounds.

actuator rate constraints and tracking error.

The role of the control surfaces in producing the commanded virtual inputs is also evident. For example, to generate positive v_y , the algorithm retracts the surfaces that would produce negative contributions (u_3, u_4) while driving u_1, u_2 upward. Conversely, for negative v_y , the roles switch. A similar logic applies for roll moments v_x , where surfaces u_2, u_3 dominate the positive direction, while u_1, u_4 dominate the negative. This role distribution is consistent with the control effectiveness structure in Eq. (55) and explains why certain surfaces repeatedly saturate depending on the sign of the demanded moment. The algorithm implicitly prioritizes the dominant axis when strong demands occur, reducing error in that channel even if moderate errors appear in the others. For instance, in phases of high pitch demand, the allocation accepts deviations in v_x to minimize the error in v_y . Such behavior could be adapted with weighting factors to impose mission-specific priorities, though in the present setup the distribution already provides a reasonable compromise.

The time histories of the rates in Fig. 20 further illustrate this behavior. Whenever a magnitude limit is reached, the corresponding rate collapses to zero, consistent with the physical limit of the actuator. This produces linear evolution in the magnitude traces and explains the sharp transitions observed in the error plots. Spikes in the rate signals occur when one surface saturates and the remaining effort is redistributed across the other actuators, causing rapid but coordinated adjustments. These interactions confirm the coupled nature of the allocation: constraints in one actuator channel propagate into others as the residual command is redistributed.

Overall, the simulation results present a consistent and physically plausible picture. The time-varying magnitude

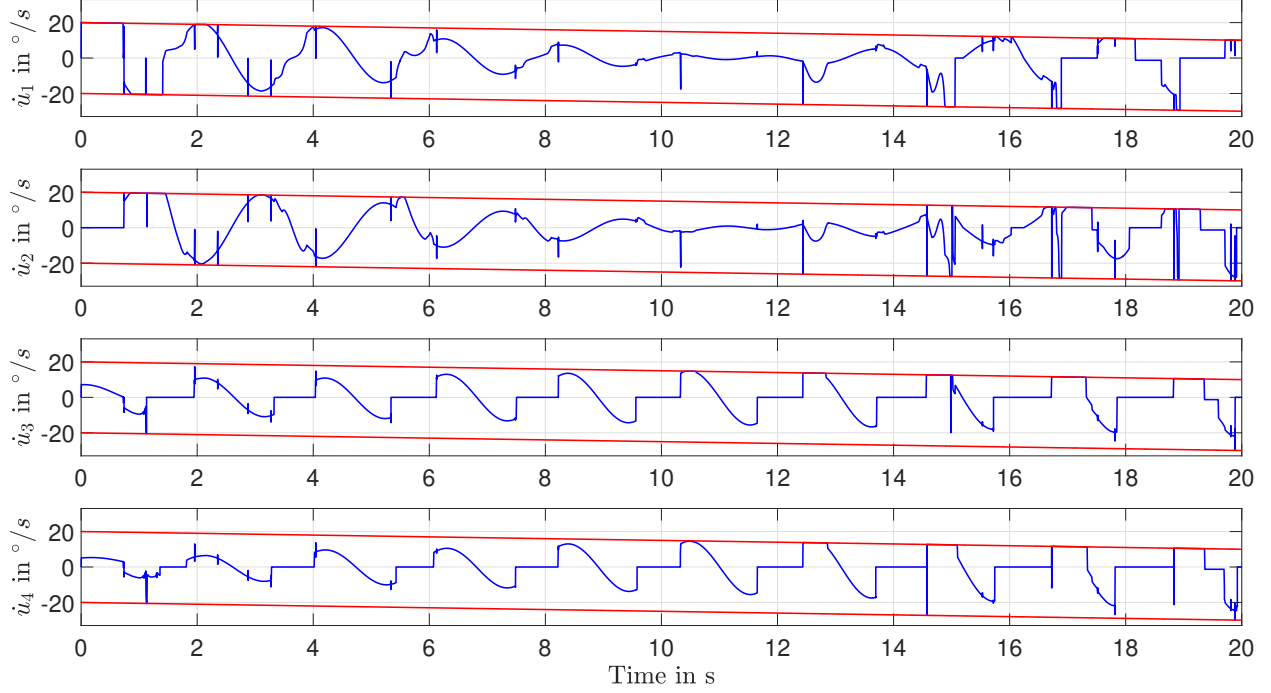


Figure 20 Computed control input rates with time-varying rate constraints. Blue: generated rates. Red: admissible bounds.

and rate bounds are respected at all times, the algorithm provides accurate tracking in feasible regions, and deviations are directly attributable to actuator limits. The prioritization behavior ensures that dominant demands are satisfied first, yielding a robust trade-off across channels. Importantly, even under dynamic and asymmetric constraints, the IDCA algorithm demonstrates reliable real-time operation and robust allocation, confirming its applicability for hypersonic flight scenarios where actuator characteristics vary significantly over time.

VII. Conclusion

In conclusion, this paper presented an iterative dynamic control allocation approach for HGVs, addressing key challenges such as asymmetric input limitations, actuator coupling, and thermal load management. Designed for computational efficiency, the approach enables real-time implementation, optimizing control distribution and reducing thermal stresses to prevent actuator saturation. Simulation results confirm its effectiveness in maintaining control authority across diverse mission profiles, meeting the stringent demands of HGV embedded systems.

Future work will incorporate state-dependent hard constraints, including limitations on achievable acceleration due to finite actuator forces. Additional studies will refine the cost function to better capture the nonlinear dynamics, further enhancing robustness and adaptability for hypersonic control applications.

References

- [1] Slayer, K. M., "Hypersonic Weapons: Background and Issues for Congress," Tech. rep., Congressional Research Service, 2023. URL <https://crsreports.congress.gov/product/pdf/R/R45811/35>.
- [2] Autenrieb, J., "Data fusion-based Incremental Nonlinear Model Following Control Design for a Hypersonic Waverider Configuration," *AIAA SciTech 2023 Forum*, 2023. <https://doi.org/10.2514/6.2023-1997>.
- [3] Bordignon, K., and Bessolo, J., "Control Allocation for the X-35B," *Biennial International Powered Lift Conference and Exhibit*, 2022. <https://doi.org/10.2514/6.2002-6020>, URL <https://arc.aiaa.org/doi/abs/10.2514/6.2002-6020>.
- [4] Johansen, T., Fossen, T., and Berge, S., "Constrained nonlinear control allocation with singularity avoidance using sequential quadratic programming," *IEEE Transactions on Control Systems Technology*, Vol. 12, No. 1, 2004, pp. 211–216. <https://doi.org/10.1109/TCST.2003.821952>.
- [5] Härkegård, O., "Dynamic Control Allocation Using Constrained Quadratic Programming," *Journal of Guidance Control and Dynamics*, Vol. 27(6), 2004. <https://doi.org/10.2514/1.11607>.
- [6] Burken, J. J., Lu, P., Wu, Z., and Bahm, C., "Two Reconfigurable Flight-Control Design Methods: Robust Servomechanism and Control Allocation," *Journal of Guidance, Control, and Dynamics*, Vol. 24, No. 3, 2001, pp. 482–493. <https://doi.org/10.2514/2.4769>.
- [7] Bordignon, K. A., "Constrained control allocation for systems with redundant control effectors," Ph.D. thesis, Virginia Polytechnic Institute and State University, 1996.
- [8] Autenrieb, J., Fezans, N., Gruhn, P., and Klevanski, J., "Towards a Control-Centric Modelling and Simulation-Framework for Hypersonic Glide Vehicles," *German Aeronautics and Space Congress (DLRK), Bremen, Germany*, German Aeronautics and Space Congress (DLRK), Bremen, Germany, 2021.
- [9] Autenrieb, J., and Fezans, N., "Nonlinear Model Following Control Design for a Hypersonic Waverider Configuration," *CEAS EuroGNC "Conference on Guidance, Navigation and Control", 3–5 May 2022, TU Berlin, Germany*, 2022.
- [10] Gruhn, P., "Design and Analysis of a Hypersonic Glide Vehicle (Original German Title: Auslegung und Analyse eines hypersonischen Gleitflugkörpers)," *Conference on Applied Research for Defense and Security in Germany*, Bonn, Germany, 2020.
- [11] Holzapfel, F., "Nonlinear adaptive control of an unmanned aerial vehicle (Original German Title: Nichtlineare adaptive Regelung eines unbemannten Fluggerätes)," Ph.D. thesis, Technische Universität München, München, Germany, Jun. 2004. URL <https://mediatum.ub.tum.de/?id=601905>.
- [12] Lombaerts, T., and Looye, G., "Design and Flight Testing of Nonlinear Autoflight Control Laws," *AIAA Guidance, Navigation, and Control Conference*, 2012. <https://doi.org/10.2514/6.2012-4982>.

[13] Bhardwaj, P., Raab, S. A., and Holzapfel, F., “Higher Order Reference Model for Continuous Dynamic Inversion Control,” *AIAA Scitech 2021 Forum*, 2021. <https://doi.org/10.2514/6.2021-1130>.

[14] Petersen, J. A. M., and Bodson, M., “Interior-Point Algorithms for Control Allocation,” *Journal of Guidance, Control, and Dynamics*, Vol. 28, No. 3, 2005, pp. 471–480. <https://doi.org/10.2514/1.5937>, URL <https://doi.org/10.2514/1.5937>.

[15] Pfeifle, O., and Fichter, W., “Cascaded Incremental Nonlinear Dynamic Inversion for Three-Dimensional Spline-Tracking with Wind Compensation,” *Journal of Guidance, Control, and Dynamics*, Vol. 44, No. 8, 2021, pp. 1559–1571. <https://doi.org/10.2514/1.G005785>, URL <https://doi.org/10.2514/1.G005785>.

[16] Ikeda, Y., and Hood, M., “An application of L1 optimization to control allocation,” *AIAA Guidance, Navigation, and Control Conference and Exhibit*, 2000. <https://doi.org/10.2514/6.2000-4566>.

[17] Bolender, M. A., and Doman, D. B., “Nonlinear Control Allocation Using Piecewise Linear Functions,” *Journal of Guidance, Control, and Dynamics*, Vol. 27, No. 6, 2004, pp. 1017–1027. <https://doi.org/10.2514/1.9546>.

[18] Huang, X., and Duan, G., “Dynamic infinity-norm constrained control allocation for attitude tracking control of overactuated combined spacecraft,” *IET Control Theory & Applications*, Vol. 13, 2019. <https://doi.org/10.1049/iet-cta.2018.5707>.

[19] Bodson, M., and Frost, S. A., “Load Balancing in Control Allocation,” *Journal of Guidance, Control, and Dynamics*, Vol. 34, No. 2, 2011, pp. 380–387. <https://doi.org/10.2514/1.51952>.

[20] Virnig, J., and Bodden, D., “Multivariable control allocation and control law conditioning when control effectors limit,” *AIAA Guidance, Navigation, and Control Conference*, 1994. <https://doi.org/10.2514/6.1994-3609>, URL <https://arc.aiaa.org/doi/abs/10.2514/6.1994-3609>.

[21] Zhang, J., Bhardwaj, P., Raab, S. A., Saboo, S., and Holzapfel, F., “Control Allocation Framework for a Tilt-rotor Vertical Take-off and Landing Transition Aircraft Configuration,” *AIAA AVIATION Forum, 2018 Applied Aerodynamics Conference*, 2018. <https://doi.org/10.2514/6.2018-3480>, URL <https://arc.aiaa.org/doi/abs/10.2514/6.2018-3480>.

[22] Härkegård, O., “Dynamic Control Allocation Using Constrained Quadratic Programming,” *Journal of Guidance, Control, and Dynamics*, Vol. 27, No. 6, 2004, pp. 1028–1034. <https://doi.org/10.2514/1.11607>.

[23] Autenrieb, J., and Fezans, N., “Flight control design for a hypersonic waverider configuration: A non-linear model following control approach,” *CEAS Space Journal*, 2024, pp. 1–24. <https://doi.org/10.1007/s12567-024-00544-0>.

[24] Li, G., Zhang, H., and Tang, G., “Flight-Corridor Analysis for Hypersonic Glide Vehicles,” *Journal of Aerospace Engineering*, Vol. 30, No. 1, 2017, p. 06016005. [https://doi.org/10.1061/\(ASCE\)AS.1943-5525.0000667](https://doi.org/10.1061/(ASCE)AS.1943-5525.0000667).

[25] An, K., Guo, Z.-Y., Xu, X.-P., and Huang, W., “A framework of trajectory design and optimization for the hypersonic gliding vehicle,” *Aerospace Science and Technology*, Vol. 106, 2020, p. 106110. <https://doi.org/10.1016/j.ast.2020.106110>.

[26] Sadien, E., Roos, C., Biroche, A., Carton, M., Grimault, C., Romana, L. E., and Basset, M., “A simple and efficient control allocation scheme for on-ground aircraft runway centerline tracking,” *Control Engineering Practice*, Vol. 95, 2020, p. 104228. <https://doi.org/https://doi.org/10.1016/j.conengprac.2019.104228>.

[27] Hohn, O., and Gruhn, P., “Thermal Investigations on a Wind Tunnel Model of a Hypersonic Missile (Original German Title: Thermaluntersuchungen an einem Windkanalmodell eines Hypersonischen Flugkörpers,” *Conference on Applied Research for Defense and Security in Germany*, Bonn, Germany, 2018.